NONLINEAR OPTICS IN HYDROGENATED AMORPHOUS SILICON (A-SI:H) WAVEGUIDES

by

Ke-Yao Wang

A dissertation submitted to Johns Hopkins University in conformity with the requirements for the degree of Doctor of Philosophy.

Baltimore, Maryland

December, 2014

Abstract

Silicon photonics combines wide-bandwidth capability afforded through optics with well-developed nano-fabrication technology, allowing for short-range communication at low cost, with low operating power and compact device footprints. In order to compete with traditional copper wiring, optical interconnects must be integrated vertically for maximum integration density. Crystalline silicon (c-Si) cannot be deposited; only epitaxially grown or bonded at high temperature thereby destroying the electronic devices and is consequently limited to single layer integration. Here we investigate a new silicon photonic material, hydrogenated amorphous silicon (a-Si:H). This material can be deposited at a low temperature $150 \sim 300°C$ within the CMOS thermal budget and is already available in the current fabrication process line.

Nonlinear optical effects allow ultra-fast time scale all-optical signal processing. However, in c-Si the nonlinear coefficient is low; therefore high input power is required for operation. A-Si, due to its unique band structure, has an order of magnitude higher nonlinear coefficient than c-Si. This high nonlinearity enables all-optical nonlinear applications at very low powers.

ABSTRACT

The first part of this dissertation will focus on the design and fabrication of the a-Si:H waveguide. The optical properties of the waveguide are measured and analyzed. Secondly, using the highly-nonlinear a-Si:H waveguide, I will discuss our demonstrations including: 1) broad-bandwidth wavelength conversion, 2) low power time-domain demultiplexing, 3) all optical signal regeneration, 4) short pulse characterization via frequency resolved optical gating (FROG), 5) broad-band optical parametric amplification and oscillation, and 6) correlated photon-pair generation.

Primary Reader: Prof. Amy C. Foster

Secondary Reader: Prof. Mark A. Foster

Acknowledgments

First, I would like to acknowledge my advisor Prof. Amy C. Foster for her guidance and financial support over the past four years. As her first graduate student, I have the privilege to witness and partake in the journey of building up a new research laboratory. As in research, Amy always enlightens me with her knowledge in integrated nonlinear optics and device fabrication. During my PhD study, she has equipped me to be an independent researcher through various training, including exploring new research topics, utilizing resources, budgeting, applying for proposals, recruiting members, teaching courses, and etc. I am also impressed by her passion for science and technology, as well as her ability to keep good balance between work and family.

I am also profoundly grateful to our closest collaborator, Prof. Mark A. Foster. His skills in optical experiment and knowledge in nonlinear and ultra-fast optics has enabled my success in many demonstrations using my device. He can always come up with novel ideas and has the insight to envision its practicality.

I want to thank my GBO committee: Prof. James Spicer, Prof. Theodore Poehler,

ACKNOWLEDGMENTS

Prof. Nina Marković, and Prof. Jacob Khurgin for their time to be on my committee. The discussion was fruitful and their comments and advice have inspired me throughout my graduate study. Especially I appreciate Prof. Jacob Khurgin, who is not only an exceptional theorist and thinker, but also an outstanding instructor and a friend. Jacob's unique remarks keep the years in graduate school fun.

I am thankful to my previous and current lab-mates both in Integrated Photonics Lab and Ultrafast and Nonlinear Photonics Group: Keith Petrillo, Walter Wall, Hongcheng Sun, Hong-Fu Ting, Amit Bhatia, Bryan Bosworth, Jasper Stroud, Kangmei Li, Michael Kossey, Iskandar Atakhodjaev, and Jaewook Shin for their help and patience with me. I am particularly grateful for Dr. Keith Petrillo, who was the very first student in Mark's group. Being the first two PhD students in this big family, we shared so many moments together through the difficulties in experiment and in lacking of resources.

In the work on the non-instantaneous nonlinearity in a-Si:H, I have the honor to collaborate with Prof. Thomas Murphy's group at University of Maryland, College Park. I am grateful to the team: Jeremiah (JJ) Wathen, Vincent Pagán, and Ryan Suess. All of them are hard-nosed scientists with strong experimental skills and sharp minds. I learned a lot of measurement skills from them. With the guidance of Prof. Murphy, we successfully carried out various experiments to understand in depth the mechanism behind the nonlinear behavior in a-Si:H.

In the collaboration with Prof. Prem Kumar's team at Northwestern University,

we have demonstrated quantum optics applications in my device. I thank Prof. Yuping Huang for his guidance and his support. I enjoyed the 24/7 non-stop experiment with their team: Vesselin Velev, Kim Fook Lee, and Abijith Kowligy. The collaboration brought me into quantum regime of optics and to another level of experimental skills and thinking.

During my first year at Johns Hopkins, I was part of the team at Prof. Marković's group in physics department. I am indebted to Prof. Nina Marković, who was kind enough to give me the opportunity to explore the beauty of low-dimensional physics. Her support and encouragement has helped me overcome my weakness and anxiety as a new foreign student. I'm also grateful to the team: Soo Hyung Lee, Atikur Rahman, Nikolaus Hartman, and Janice Guikema. I learned a lot from each one of them. Although I could not work with them to the end in my PhD journey, their help and support for me cannot be overstated.

With the help of the ECE department staff, Janel Johnson, Cora Mayenschein, and Debbie Race, I can focus on my own research without worrying too much about non-research duties. Their promptness in response and tireless effort indeed contributes to my accomplishment in pursuing the degree.

I also acknowledge the financial support from the Defense Advanced Research Projects Agency (DARPA) and start-up funds from Johns Hopkins University.

I thank my brothers and sisters in LIFE fellowship, AFC fellowship, and Chinese Christian Church of Baltimore. They have walked with me through my spiritual

journey.

Finally, I'm enormously indebted to my family: my wife Lingling, my mom and dad and sister. I would not have finished my study and obtain my degree without their support. My ultimate gratitude be to my Lord Jesus Christ, who guides me and encourages me, not only during my stay in US, but also throughout my life; not only in research, but also in every other aspect of my life. He has brought true hope and real purpose to my life. May my life glory Him.

Contents

Abstract **ii**

Acknowledgments **iv**

List of Tables **xii**

List of Figures **xiii**

1 Introduction **1**

1.1 Overview 1

1.2 Hydrogenated amorphous silicon (a-Si:H) 4

1.3 Waveguide design and fabrication 5

1.3.1 Dispersion engineering 5

1.3.2 Device fabrication 7

1.3.3 Waveguide loss 10

1.3.4 Sample stability 10

1.4 Optical nonlinear properties 11

1.4.1 Nonlinearity characterization using FWM efficiency 13

1.4.2 Nonlinearity characterization using inverse transmission and self-phase modulation 14

1.4.3 Comparison 17

2 Wavelength conversion **21**

2.1 Introduction 21

2.2 Continuous-wave (CW) wavelength conversion 22

2.3 Telecommunication data rate wavelength conversion 24

2.4 Modeling the conversion efficiency 26

2.5 Conclusion 27

3 Optical time demultiplexing **28**

3.1 Introduction 28

3.2 Experiment 32

3.3 Results 34

3.4 Conclusion 37

4 All optical signal regeneration **39**

4.1 Introduction 39

4.2 Waveguide design and fabrication 42
4.3 Experimental setup 42
4.4 Results 43
4.5 Discussion 46
4.6 Conclusion 47

5 Short pulse characterization 48

5.1 Introduction 48
5.2 SHG-like FWM-FROG 51
5.3 THG-like FWM-FROG 55
5.4 Conclusion 61

6 Optical parametric amplifier and oscillator 62

6.1 Introduction 62
6.2 Ultra-broad bandwidth a-Si:H optical parametric gain 63
6.3 A-Si:H GHz rate parametric gain 66
6.4 A-Si:H Optical parametric oscillator 70

7 Correlated photon-pair generation 78

7.1 Introduction 78
7.2 Experiment 79
7.3 Results 81
7.4 Discussion 85

8 Conclusion and future work **87**

8.1 Conclusion 87

8.2 Future work 88

Bibliography **89**

Vita **108**

List of Tables

1.1 Nonlinear properties of different materials at $\lambda = 1550\,nm$ 20

3.1 OTDM demultiplexing using different platform 37

6.1 Optical gain bandwidth in various integrated demonstrations 66

List of Figures

1.1 Optical communication applications are moving toward short haul systems (from [1]) . . . 2
1.2 Future 3-D photonic circuit envisioned by researchers in IBM (from IBM website), Columbia University (Bergman's group website), and Cornell Univeristy (Lipson's group [2]) . . . 4
1.3 Structure of a-Si:H. The dangling bonds cause high optical loss. Hydrogen passivation can terminate the bonds and greatly reduce the optical loss.(from http://www.eere.energy.gov/) . . . 5
1.4 Efficient four-wave mixing (FWM) process requires energy and momentum conservation . . . 6
1.5 Group velocity dispersion as a function of wavelength for different waveguide geometries . . . 7
1.6 Pictures of the equipment for the waveguide fabrication (from NIST website) . . . 8
1.7 A-Si:H waveguide fabrication processes . . . 9
1.8 (Left)simulated mode profile of the 215 nm × 500 nm a-Si:H waveguide. (Right) scanning electron microscope image of the fabricated waveguide before cladding. There is 150 nm silicon dioxide hard mask on top of the waveguide. . . . 9
1.9 Experimental setup for cutback method to characterize the linear loss and the coupling loss of the waveguide. . . . 10
1.10 Linear propagation loss and fiber-to-waveguide coupling loss of the fabricated waveguide measured by cut-back method. . . . 11
1.11 Experimental setup for CW four-wave mixing. . . . 14
1.12 Experimental setup for inverse transmission and self-phase modulation 15
1.13 Inverse transmission as function of input peak power for c-Si (left) and a-Si:H (right) . . . 16
1.14 Measured and modeled self-phase modulation spectrum evolution for c-Si . . . 17

1.15 Measured and modeled self-phase modulation spectrum evolution for a-Si:H. 18

2.1 Schematic of experimental setup for CW four-wave mixing measurement. 22
2.2 (Left)the overlay of wavelength dependent FWM when the pump is fixed at 1541 nm, and the signal is swept from 1470 nm to 1540 nm. (Right)Theoretical (curve) and experimental (dots) conversion efficiency as functions of converted wavelength for the TE-mode. A conversion efficiency of approximately -30 dB is measured over the 150 nm bandwidth including the symmetric lobe to the short wavelength side. The variation in conversion efficiency is in part due to the Fabry-Perot effects in the waveguide. 23
2.3 Telecommunication data rate (10 GHz) four wave mixing (FWM) experimental setup for a-Si:H waveguide. 24
2.4 (Left) Sample 10-GHz four-wave mixing spectrum from a 8 mm a-Si:H waveguide when pump peak power is 8 mW. (Right) Maximum conversion efficiency as function of pump peak power. Dots represent the measured conversion efficiency and solid line shows the expected result from a quadratic relationship. Saturation due to nonlinear loss is observed when input power is greater than $\sim$10 dBm. 25

3.1 Schematic of WDM and OTDM. OTDM is a spectral efficient scheme. But the demultiplex requires ultrafast process that's beyond the limitation of electronics. 29
3.2 Schematic ultrafast nonlinear switch. 30
3.3 Hydrogenated amorphous silicon is a highly nonlinear material that can be deposited at low temperatures allowing for the creation of energy-efficient sophisticated three-dimensionally integrated ultrafast photonic processing circuits such as the demultiplexer depicted here. . 31
3.4 Experimental setup for 160-to-10 Gb/s all-optical demutiplexing using an a-Si:H waveguide (EOM: electro-optical modulator. TBPF: tunable bandpass filter. MUX: Mach-Zehnder multiplexer. PC: polarization controller. HNLF: highly nonlinear fiber. WDM: wavelength division multiplexer. PD: photo-detector. BERT: bit-error rate tester.). Inset: auto-correlation traces of 160-Gb/s signal and 10-GHz pump at the input of the waveguide. 32
3.5 (a) Input and output spectra of the demultiplexing process in the 6-mm-long a-Si:H waveguide showing the input 160-Gb/s signal, the 10-GHz pump, and the generated 10 Gb/s idler. (b) The BER measurement of the 160 Gb/s to 10 Gb/s demultiplexing of all 16 channels and 10 Gb/s back-to-back (B2B). Error-free operation (10^{-9}) is achieved with 4- to 5-dB power penalty. Inset: demuxed eye diagram. 35

3.6 Bit-error rate as a function of coupled peak pump power. Error-free operation (10-9) is achieved with a 17-dBm (50 mW) peak switching power. 36

4.1 Schematic of Mamyshev 2R regeneration. Utilizing the self-phase modulation (SPM) in a highly nonlinear medium followed by an optical filter can reshape the degraded optical signals. 41
4.2 2R regenerator re-amplify and re-shape the degraded optical pulses . 41
4.3 Experimental setup for 2R regeneration in a-Si:H waveguide. 43
4.4 (a)SPM-broadened spectra of the a-Si:H waveguide when input peak power is 0.4 W and 5.2 W. The spectrum of the filter has 100GHz bandwidth. High power pulses will spectrally broaden into the filter range.(b)Measured power transfer function of the 2R regenerator. The output power saturates at 5 W. 44
4.5 (a) The BER of regenerated signal and back-to-back (B2B) signal. The regenerated signal shows 2 dB received power improvement. (b) the eye diagram of input and output of the regenerator at same power level. The histograms show the samples in the shaded area which represents the distributions noise in logical ones and zeros 45

5.1 A time delayed replica of the pulse can gate out a portion of the original pulse. By saving the spectrum for different time delay can generate a spectrogram and an algorithm can calculate the amplitude as well as phase of the pulse. 49
5.2 Schematic of experimental setup for SHG-like FWM-FROG measurement. Two different pulses under test are generated by a mode-locked fiber laser with or without the compression stage. Inset: optical spectrum at the output of the a-Si:H waveguide. (PUT: pulse under test. HNLF: highly nonlinear fiber. VOA: variable optical attenuator. WDM: wavelength division multiplexer. EDFA: erbium-doped fiber amplifier. OBPF: optical bandpass filter. PC: polarization controller. OSA: optical spectrum analyzer.) 51
5.3 Pulse characterization of PUT 1 (left column), and PUT 2 (right column). (a),(e) Optical spectrum at the output of the waveguide. (b),(f) Measured and retrieved FROG. (c),(g) FROG retrieved autocorrelation and spectrum in comparison to the measurement. (d),(h) Retrieved amplitude and phase in both time and frequency domain. 53
5.4 A block diagram of the cascaded FWM THG FROG. A nonlinear copy creation stage develop a replica of the pulse to be measured on a second wavelength. The two signals are isolated and delayed with respect to each other prior to mixing. The result from the mixing is read on a spectrum analyzer. 56

5.5 The experimental setup of cascaded FWM stages for THG FROG (PM: phase modulator. D-38 fiber: corning vascade S2000 fiber. MLFL: mode locked fiber laser). Insets (a), (b), and (c) show the spectrum of the experimental setup after the initial HNLF stage, before the waveguide, and after the waveguide respectively where BWres is the bandwidth resolution of the OSA. 57
5.6 The experimental results where starting from left to right the columns show experimental FROG spectrogram traces, the reconstructed traces, the temporal reconstruction (solid) and its phase (dashed) with the corresponding experimental (dashed) and recovered (solid) autocorrelation in the inset, and the spectral reconstruction (solid) with its phase (dashed) and the measured spectrum (dotted) for the transform limited (top row), anomalously chirped (second row), normally chirped (third row), and self phase modulation with compression cases (bottom row). 59

6.1 Experimental setup for the broad band parametric amplification measurement. (OBPF: optical bandpass filter. EDFA: erbium-doped fiber amplifier. HNLF: highly nonlinear fiber. PC: polarization controller. WDM: wavelength division multiplexer. OSA: optical spectrum analyzer) 64
6.2 (a) Optical spectrum with pump on (blue) and pump off (red). (b) On/off gain as function of wavelength when pump is at 1558 nm. . . 65
6.3 Schematic of experimental setup for 1-GHz optical parametric amplification measurement. (EOM: electro-optical modulator. WDM: wavelength division multiplexer. EDFA: erbium-doped fiber amplifier. PC: polarization controller. OSA: optical spectrum analyzer.) 67
6.4 On-chip signal gain and idler conversion at different repetition rates. . 68
6.5 a) Measured optical spectra of optical parametric amplification for various signal wavelengths. b) On-chip gain/idler conversion as function of wavelength with pump at 1550 nm. c) On-chip gain/conversion as function of coupled peak pump power. 70
6.6 Approaches for achieving silicon-based optical light source [3–6]. . . . 71
6.7 (a) Experimental setup for the optical parametric oscillator. (PC: polarization controller. WDM: wavelength division multiplexer. OSA: optical spectrum analyzer. PBS: polarization beam splitter. $\lambda/2$: half-wave plate. Red line: single mode fiber). (b) Single pass parametric fluorescence for different pump power. (c) Optical spectrum of the OPO when oscillation wavelength is at 1460 nm. 72

6.8 (a) Output energy of OPO as function of coupled pump energy. The oscillation threshold is 1.53 pJ with a slope efficiency of 4.4%. Inset: output spectrum as function of coupled pump energy. (b) Cross-correlation trace between oscillation (1476 nm) and a strong 1.5 ps pump. The de-convolved pulse width for oscillation output is 1.1ps. . 74
6.9 Overlaid tuning spectra of the oscillation mode at short wavelength side (1370 nm $\sim$ 1515 nm), and long wavelength side (1600 nm $\sim$1810 nm) for a 1558-nm pump laser. 75
6.10 Wavelength extension through cascaded FWM. (a) Optical spectrum with increased pump power when +1 mode is on resonance. Cascaded FWM generates idlers at +2, -1, -2, -3, -4 modes. (b) Oscillating wavelength (+1 mode) near 1700 nm with cascaded FWM (+2 mode) for light generation at $\sim$1900 nm. 75
6.11 Cross-correlation trace of the oscillation mode (1467 nm) with a 250-fs reference pulse. The de-convolved pulse width for the oscillation mode is 300 fs assuming a $sech^2$ shape. The side peak in the trace is the cross-correlation of the cascaded FWM idler. (Inset: the output spectrum of the reduced net dispersion OPO cavity. The bandwidth of the oscillation mode is greater than 30 nm, allowing ultra-short pulse generation.) 76

7.1 Experimental setup for photon-pair generation. (WDM: wavelength division multiplexer, FPC: fiber polarization controller, FPBS: fiber polarization beam splitter) 81
7.2 Singles counts per pump pulse as a function of pump photons for the case of 20 nm detuning. Both the Stokes and anti-Stokes data are shown along with their respective fits. Also shown is a per-pulse photon-number curve assuming no Raman scattering and only FWM. The statistical error bars for the experimental data are within the markers. 82
7.3 (a) Dark-count subtracted CAR versus the pump photon number per pulse. The highest CAR for the 15 nm (20 nm) detuning is 399 (168). (b) Dark-count subtracted coincidence and accidental coincidence count per pump pulse as a function of the peak pump power for both channels. 84

Chapter 1

Introduction

1.1 Overview

With the increasing demand for larger communication bandwidths, optics enables the possibility of high speed data transmission at all length scales of communication. Long haul optical communications has been widely implemented using the well-developed fiber technology and state-of-the-art photonic components. Over the past few decades, there has been a trend of utilizing optics for short range communication systems such as board-to-board, chip-to-chip and on-chip interconnects [1] (Fig. 1.1). In order to compete with traditional copper wiring, optical interconnects must utilize its full bandwidth, reduce the cost and power, and increase the packing density. Silicon photonic interconnects have the potential to overcome the limited bandwidths of traditional electronic communications, while taking advantage

of the well-developed microelectronic fabrication techniques. Using silicon as a platform, photonic and microelectronic devices can be monolithically integrated on-chip, utilizing both the versatility of microelectronics and the large bandwidth capability of photonics. Silicon is the dominant material in the electronics industry, and has recently emerged as the material of choice for photonic applications due to its beneficial optical properties [7]. Many companies such as Intel and IBM have demonstrated high data rate optical interconnect using silicon photonics platform; Gb/s optical transceiver has become commercially available by various vendors.

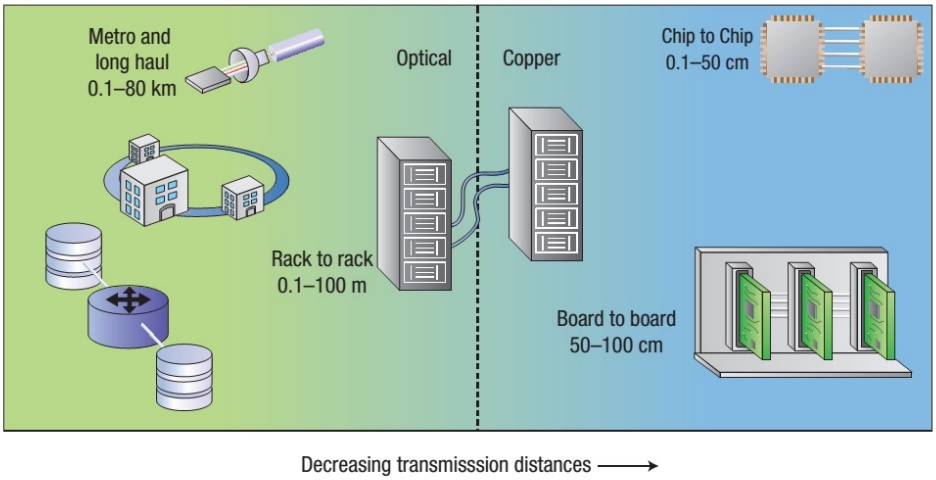

Figure 1.1: Optical communication applications are moving toward short haul systems (from [1])

However, if we look at the demonstration by IBM [8], photonics devices exist at the same SOI (silicon-on-insulator) layer as the transistors, taking away precious real-estate from the micro-electronic devices. Therefore, the photonics is only limited to single layer in a 2-D manner. In a traditional integrated circuit, copper intercon-

nects can be stacked vertically and be processed at the back-end. Therefore, in order to replace the copper wires, photonic wires must have superior stacking capability. For this reason, researchers have envisioned future 3-D integrated photonic circuits where the photonic layers can be on top of the electronic devices (Fig 1.2). However, the vast majority of research utilizes crystalline silicon (c-Si), which requires high temperature annealing, material bonding, or high temperature epitaxial growth to define the photonic layer, therefore vertical stacking of c-Si is not possible within the CMOS (Complementary metal-oxide-semiconductor) compatible thermal budget. In this dissertation I will investigate a new photonic material, a-Si:H (hydrogenated amorphous silicon) and explore its application for all-optical processing using nonlinear optical effects. A-Si:H has high refractive index contrast with silica so the photonic device footprint can be compact. The material itself can be easily deposited at low temperature ($150 \sim 300°C$) using standard plasma-enhanced chemical vapor deposition (PECVD) thereby allowing vertical stacking of photonic layers. A-Si:H is available in standard CMOS fabrication lines and is compatible with back-end processes. At the same time, nonlinear optical processes enable generation, modulation, transmission, and detection of photons at ultrafast timescales, and the validation of a-Si:H as a highly nonlinear material thereby demonstrates its potential to achieve highly-functionalized optoelectronic devices.

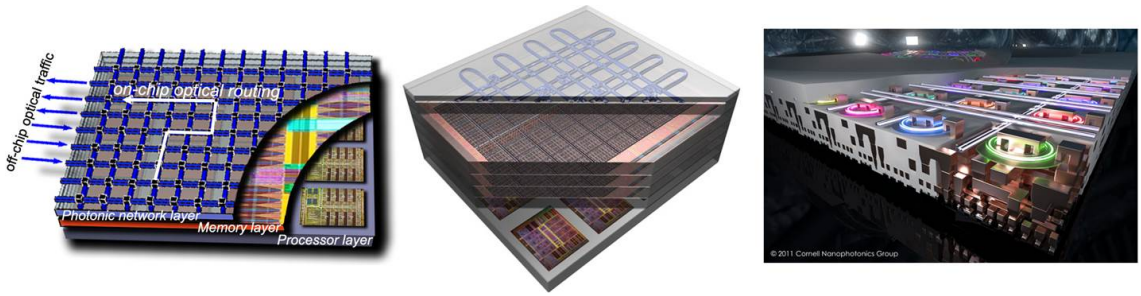

Figure 1.2: Future 3-D photonic circuit envisioned by researchers in IBM (from IBM website), Columbia University (Bergman's group website), and Cornell Univeristy (Lipson's group [2])

1.2 Hydrogenated amorphous silicon (a-Si:H)

A-Si (the non-hydrogenated form of amorphous silicon) is a CMOS compatible material with refractive index of ~ 3.45 at wavelength of 1550nm. It has been widely used in fabrication lines as the precursor for p-Si gate. The high optical loss of a-Si is primarily due to the absorption of the dangling bonds and therefore very limited optical application has been shown. It has been found that the dangling bonds in a-Si can be terminated by passivated hydrogen (Fig. 1.3), and the optical propagation loss can be as low as 2 dB/cm for highly confined single mode waveguide [9]. More recently, with the advancements in fabrication, sub 1 dB/cm a-Si:H waveguides were demonstrated [10].

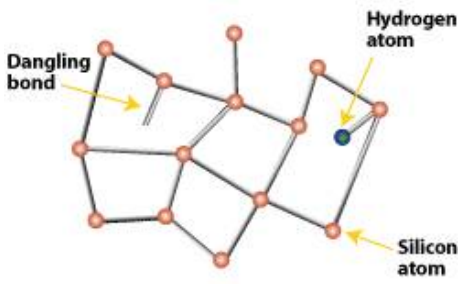

Figure 1.3: Structure of a-Si:H. The dangling bonds cause high optical loss. Hydrogen passivation can terminate the bonds and greatly reduce the optical loss.(from http://www.eere.energy.gov/)

1.3 Waveguide design and fabrication

1.3.1 Dispersion engineering

The primary optical nonlinear process in the applications presented in this dissertation is four-wave mixing (FWM) where two pump photons are converted into an idler photon and signal photon. This process can generate photons at different wavelengths and simultaneously amplify an input signal. This parametric process requires both energy and momentum conservation (Fig. 1.4). Energy conservation determines the wavelength (frequency) of the new generated idler such that $\omega_{pump1} + \omega_{pump2} = \omega_{signal} + \omega_{idler}$; momentum conservation determines the efficiency (bandwidth) of the FWM process. The physical concept behind momentum conservation is that the phase of each new generated idler photon along the length of the nonlinear medium must be in-phase with the previous generated idler photons, otherwise they destructively interfere and the output power is limited at the given

frequency. The phase can be controlled by the velocity of light traveling along the medium for different wavelengths. The phase mismatch can be described by:

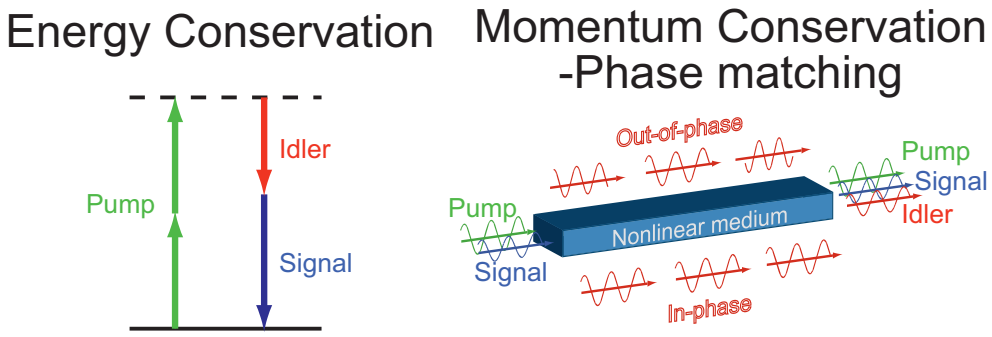

Figure 1.4: Efficient four-wave mixing (FWM) process requires energy and momentum conservation

$$\Delta k = 2\gamma P_{pump} - 2k_{pump} + k_{signal} + k_{idler} \tag{1.1}$$

where $\gamma = 2\pi n_2/\lambda A_{eff}$ is the effective nonlinearity. $k_{pump}, k_{signal}, k_{idler}$ are the propagation constants of pump, signal, and idler. The first term in the right hand side of the equation comes from the nonlinear phase shift. In the small gain regime where the contribution from the nonlinear phase shift is limited, the FWM bandwidth is determined by the dispersion at the pump wavelength and can be approximated by [11]:

$$\Omega_{FWM} = \left[\frac{4\pi}{\beta_2 L}\right]^{1/2} \tag{1.2}$$

Therefore, in small-gain regime, in order to achieve wide bandwidth operations, the group-velocity dispersion (D) should be near zero at the pump wavelength in the case of pump-degenerate FWM. For large gain applications, slightly anomalous group

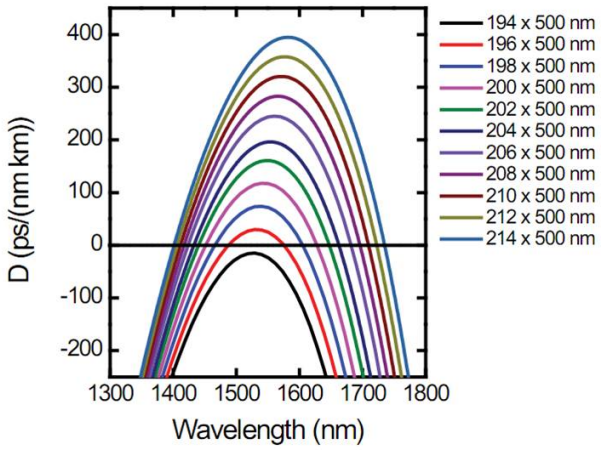

Figure 1.5: Group velocity dispersion as a function of wavelength for different waveguide geometries

velocity dispersion is necessary to compensate for the nonlinear phase shift. One of the benefits of high-index contrast waveguides is that the waveguide dispersion can be carefully controlled to overcome the material dispersion [12]. We have calculated the group velocity dispersion for the a-Si:H waveguide with 500 nm width and various thicknesses. The dispersion curves are shown in Fig 1.5. As will be evident in the experimental demonstrations throughout this dissertation, we chose a 196 nm $\times$ 500 nm waveguide (near ZGVD at 1550 nm) for continuous-wave (CW) or high repetition rate (10 GHz) applications. For the large-gain regime we use 215 nm $\times$ 500 nm waveguide ($D \simeq 350\, ps/(nm \cdot km)$) to achieve wide gain bandwidth.

1.3.2 Device fabrication

The a-Si:H nanowaveguide is fabricated using standard microelectronics fabrication techniques at the Center for Nanoscale Science and Technologys NanoFab at

Figure 1.6: Pictures of the equipment for the waveguide fabrication (from NIST website)

the National Institute of Standards and Technology (Fig. 1.6). The whole fabrication process is depicted in Fig 1.7. After the standard RCA clean, the a-Si:H film is deposited by plasma-enhanced chemical vapor deposition (Unaxis 790) on a silicon wafer with 3 μm buried oxide (BOX). The a-Si:H film deposition chamber parameters are: a gas flow of 1200 sccm made up of helium with 5 % silane is kept at a pressure of 900 mT with 50 W RF power. The substrate is maintained at 300°C during the deposition. A thin layer of silicon dioxide ($\sim$ 150 nm) is deposited as a hard mask to reduce effects from direct etching with organic resists. Electron-beam lithography (JEOL JBX 6300-FS) followed by chlorine-based inductively coupled plasma (ICP) etching (Unaxis SHUTTLELINE ICP) is used for waveguide patterning. A thick silicon dioxide layer ($\sim 1\mu m$) was deposited over the waveguide for cladding and for

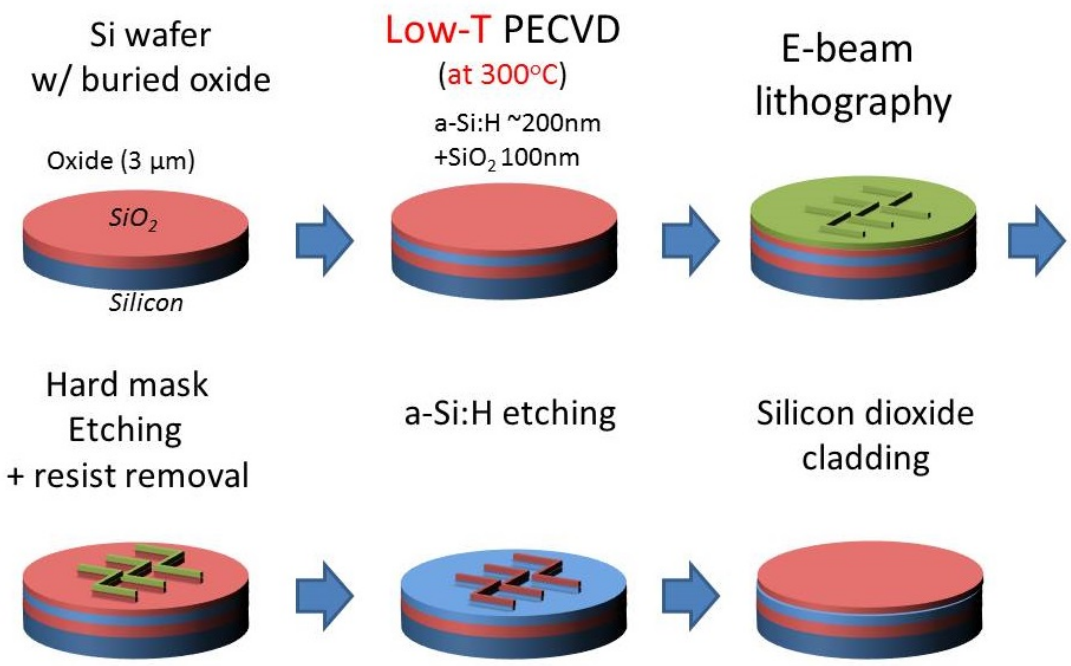

Figure 1.7: A-Si:H waveguide fabrication processes

protection. Inverse adiabatic tapers on both ends of waveguide are made for optical coupling [13]. The scanning electron microscpoe image of the fabricated waveguide and the modeled transverse-electric mode profile are shown in Fig. 1.8

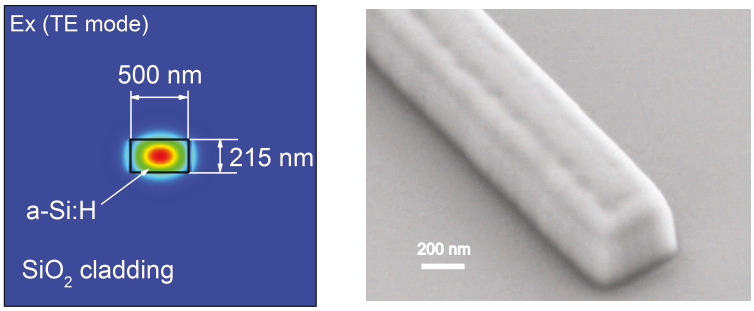

Figure 1.8: (Left)simulated mode profile of the 215 nm × 500 nm a-Si:H waveguide. (Right) scanning electron microscope image of the fabricated waveguide before cladding. There is 150 nm silicon dioxide hard mask on top of the waveguide.

1.3.3 Waveguide loss

The linear propagation and coupling loss are measured by the "cutback method" as shown in Fig. 1.9, where waveguides with different lengths are fabricated on the same die and the total loss for each individual waveguide is measured. The coupling loss for each waveguide is assumed to be the same and by measuring the increase in total loss for longer waveguides, the linear propagation loss can be determined. The total measured loss as function of waveguide lengths are plotted in Fig. 1.10. The slope of the line represents the propagation loss and from the intercept values at the zero length, the coupling loss can be extrapolated. Using this method, we characterize the propagation loss of our a-Si:H waveguide to be 3.2 dB/cm in TE-mode and the coupling loss from lensed fiber to waveguide to be about 6.5 dB per facet.

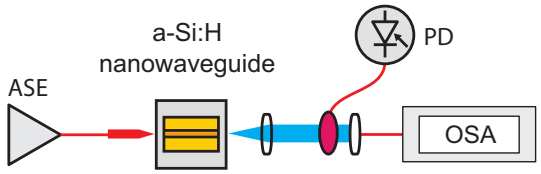

Figure 1.9: Experimental setup for cutback method to characterize the linear loss and the coupling loss of the waveguide.

1.3.4 Sample stability

There are reports [14] indicating that the a-Si:H waveguide can degrade due to the so-called Staebler-Wronski effect [15]. During our experiment, we find that the samples degrade over time (in few months) after exposure to visible light. This degra-

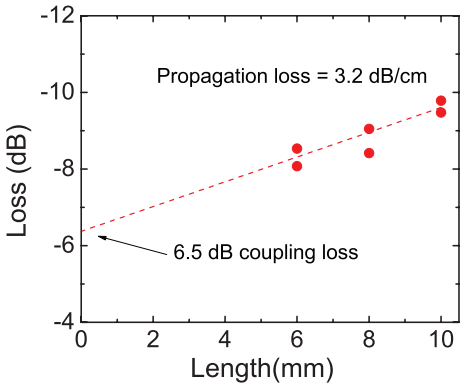

Figure 1.10: Linear propagation loss and fiber-to-waveguide coupling loss of the fabricated waveguide measured by cut-back method.

dation is well-studied and could be avoided by isolating the sample from visible light or adding an opaque cover for packaging. Critically, we did not observe waveguide damage by the telecommunication wavelength light used in the experiments. We found no correlation between degradation and exposure to high average power infrared light in the waveguide.

1.4 Optical nonlinear properties

Higher order susceptibility ($\chi^{(2)}$, $\chi^{(3)}$, ...) can become prominent when the injecting light intensity is strong enough, and is particularly critical in very high confinement regimes such as integrated waveguides. These higher order terms can contribute to the change of optical properties of a material thereby modifying the property of light. This process (electronic response) occurs usually in an ultra-fast scale about hundreds of tera-hertz and can be used for ultra-high speed signal processing. Com-

mon CMOS-compatible materials are centro-symmetrical so no second order nonlinearity ($\chi^{(2)}$) is available. Third-order nonlinearity ($\chi^{(3)}$) is typically small but can be enhanced by strong confinement of light. The real part and imaginary part of nonlinear refractive index can be related to ($\chi^{(3)}$) by:

$$n_2 = \frac{3Re[\chi^{(3)}]}{8n}, \qquad \alpha_2 = -\frac{3\omega_0 Re[\chi(3)]}{4nc} \tag{1.3}$$

The effective refractive index becomes:

$$n = n_0 + n_2 I - i\frac{\lambda}{4\pi}(\alpha_0 + \alpha_2 I) \tag{1.4}$$

where the real part (n_2) contributes phase shift, and the imaginary part (α_2) induces nonlinear loss. It is useful to define a nonlinear figure-of-merit to describe the amount of nonlinear phase shift within one absorption length [16]:

$$FOM = \frac{n_2}{\lambda\alpha_2} \tag{1.5}$$

For a nonlinear device to be useful, the FOM of higher than 1 is desirable. It's also useful to obtain the information of free carrier absorption that is typically induced by nonlinear loss (two-photon absorption). We characterize the nonlinearity of our a-Si:H waveguide using various techniques. The details are provided in the following sections.

1.4.1 Nonlinearity characterization using FWM efficiency

To accurately determine the nonlinear refractive index of the material, we perform FWM (Fig. 2.1) in our device in the extremely low input pump power regime ($\sim 300\mu W$) where the nonlinear loss mechanisms are deemed negligible. In this regime, the maximum conversion efficiency can be described by [11]:

$$Max(CE) = sinh^2(\gamma P_{pump} L_{eff}) \tag{1.6}$$

and

$$\gamma = \frac{2\pi n_2}{\lambda A_{eff}} \tag{1.7}$$

where γ is the effective nonlinearity of the device, n_2 is the nonlinear refractive index, λ is the wavelength of light, P_{pump} is the pump power in the waveguide, L_{eff} is the effective length of the waveguide ($(1 - e^{-\alpha_0 L})/\alpha_0$), and A_{eff} is the effective optical mode area . Using this relation, we extract the nonlinear refractive index of our a-Si:H to be $n_2 = 3.1 \times 10^{-13} cm^2/W$ (or $\gamma = 1260 W^{-1} m^{-1}$). This high nonlinear refractive index implies the potential for efficient, low power nonlinear applications using a-Si:H waveguides.

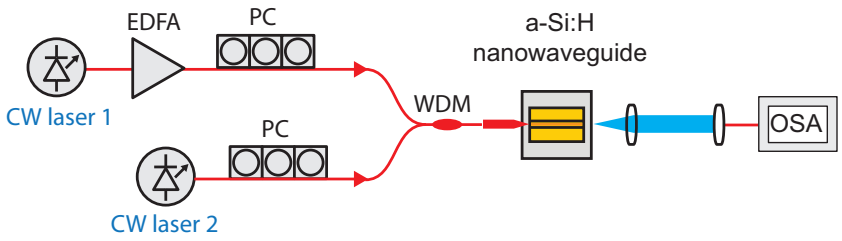

Figure 1.11: Experimental setup for CW four-wave mixing.

1.4.2 Nonlinearity characterization using inverse transmission and self-phase modulation

Nonlinear loss in silicon material is mostly dominated by two-photon absorption (TPA) whereby two photons can be simultaneously absorbed via χ_3 nonlinearity. The imaginary part of the nonlinear refractive index, α_2 can lead to inefficient nonlinear process and further induces free carriers that can absorb injecting photons. The nonlinear loss can be measured by the transfer function of the waveguide. The imaginary part of the nonlinearity can be extracted from the linear fit of the inversion transmission function.

$$\frac{1}{T} = \frac{P_{in}}{P_{out}} = e^{\alpha_0 L}(1 + \frac{\alpha_2}{\Gamma A_{eff}} L_{eff} P_{in}) \tag{1.8}$$

where T is transmission, P_{in} and P_{out} represent input and output power; L_{eff} is the effective propagation length of the waveguide. Using the experimental setup shown in Fig. 1.12, we can measure the inverse transmission as function of input power for both c-Si and a-Si:H waveguide.

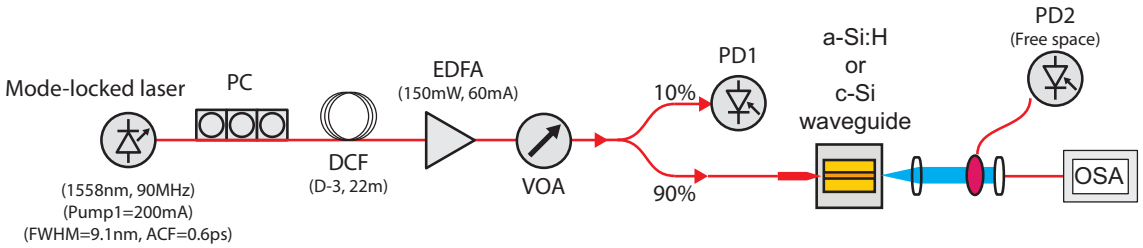

Figure 1.12: Experimental setup for inverse transmission and self-phase modulation

The results are shown in Fig. 1.13. At low input power, a linear fit extract the two photon absorption to be 1.18 cm/GW for c-Si and 1.43 cm/GW for a-Si:H. It is notable that for a-Si:H, inverse transmission curve up at high input powers. This is due to higher order absorption (three photon absorption) or strong free carrier effects. The recorded self-phase modulation spectrum for c-Si and a-Si:H waveguides as function of input power and the simulation results using split-step Fourier method (SSFM) are shown in Fig. 1.14 and Fig. 1.15 for comparison. The n_2 can be estimated by fitting the simulation parameters. The n_2 of a-Si:H ($5\times10^{-13}cm^2/W$) is about one order of magnitude higher than c-Si. This value is different from the results obtained by FWM conversion efficiency. This is partly because the two samples under test were prepared separately and therefore there exist variations in the material properties.

The modeling of the pulse propagation is achieved by numerically solving the Nonlinear Schordinger Equations (NLSE). The equation to describe an optical pulse propagating through a medium is given by:

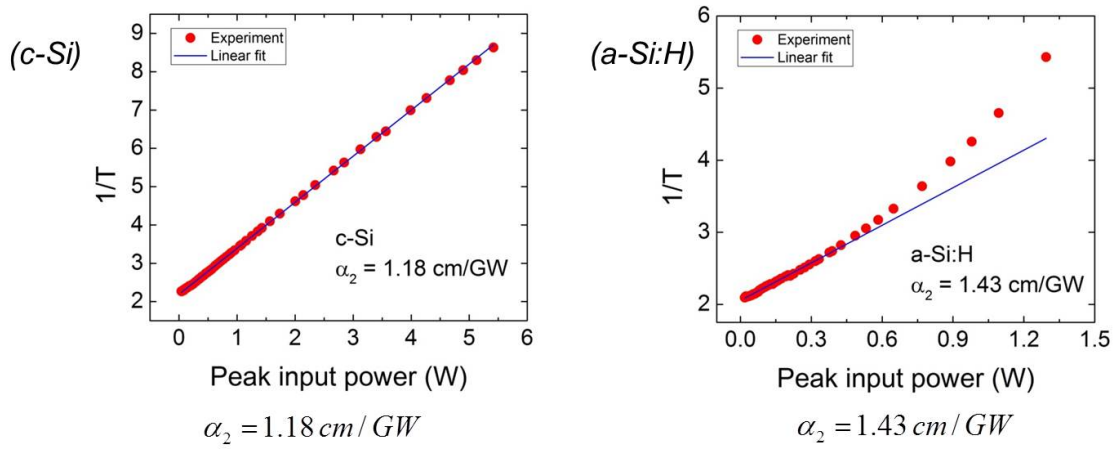

Figure 1.13: Inverse transmission as function of input peak power for c-Si (left) and a-Si:H (right)

$$\frac{\partial}{\partial z}A(t,z) = -\left[\frac{\alpha}{2} + i\frac{\beta_2}{2}\frac{\partial^2}{\partial t^2}\right]A(t,z) + \left[i\gamma - \frac{\alpha_2}{2}\right]|A(t,z)|^2 A(t,z) - \left[ik_{FCD} + \frac{\sigma_{FCA}}{2}\right]N(t,z)A(t,z) \tag{1.9}$$

where $A(t,z)$ is the pulse electric field; α is the linear propagation loss coefficients ; α_2 is the two photon absorption coefficient; β_2 is the group velocity dispersion of the waveguide;γ is the effective nonlinearity of the waveguide. σ_{FCA} and k_{FCA} are the free carrier absorption and dispersion coefficients.$N(t,z)$is the total number of free carriers and is given by:

$$\frac{\partial N(t,z)}{\partial t} = \frac{\alpha_2}{2h\nu}|A(t,z)|^4 - \frac{N(t,z)}{\tau_{eff}} \tag{1.10}$$

where τ_{eff} is the effective free carrier lifetime; h is Planck's constant. These two equations can be numerically solved by standard split-step Fourier method to model

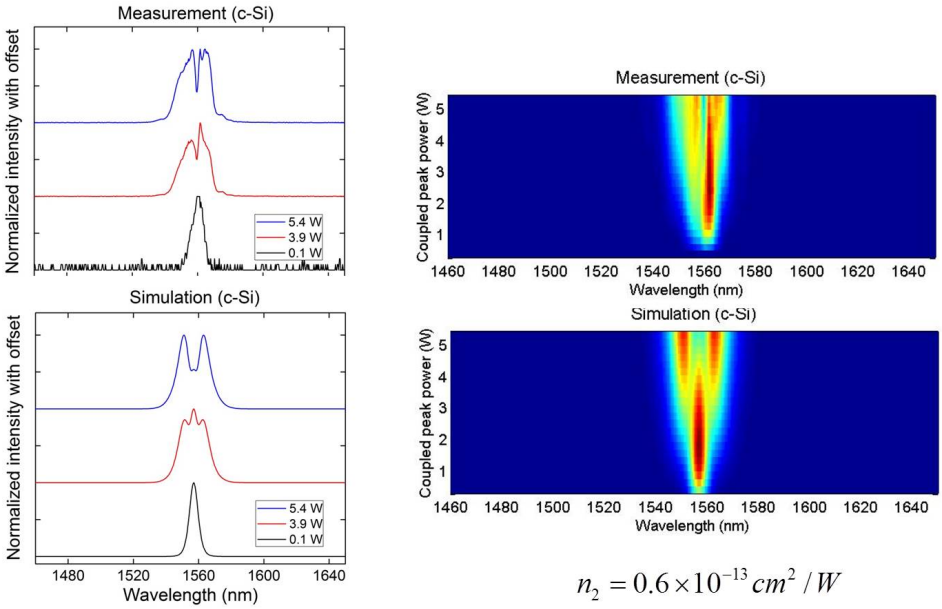

Figure 1.14: Measured and modeled self-phase modulation spectrum evolution for c-Si

the pulse propagation behavior. The simulated spectra for c-Si and a-Si:H are shown in Fig. 1.14 and Fig. 1.15.

1.4.3 Comparison

Using these two methods, we can obtain n_2, α_2 and the nonlinear FOM of the a-Si:H waveguide. Table 1.1 shows the comparison of the nonlinear properties of different materials. This table shows the potential of a-Si:H as CMOS-compatible platform for nonlinear applications. The values of nonlinearity in a-Si:H reported by different group vary dramatically. This is due to the deposited nature of the material. The material properties (including molecular density and hydrogen concentrations)

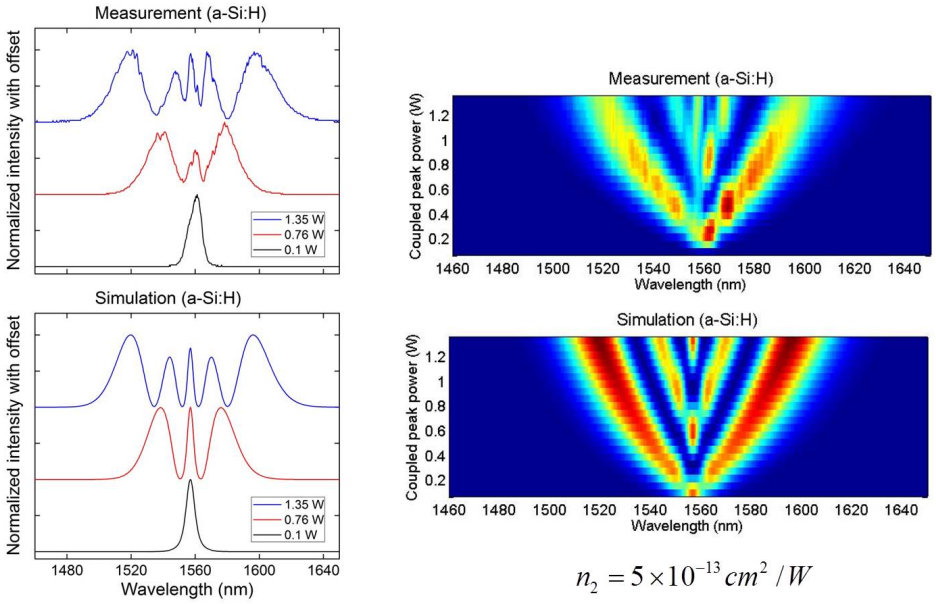

Figure 1.15: Measured and modeled self-phase modulation spectrum evolution for a-Si:H.

may be different due to deposition conditions. However, we can see most of the reported values show a stronger nonlinearity and higher nonlinear FOM than c-Si.

Although the origin of this high nonlinear FOM is still not clear yet, there exist some possible explanations on why a-Si:H has such different nonlinear behavior than c-Si [17,18]. One of the most plausible explanations is that the change of both indirect and direct band structures alter the optical properties in a-Si:H. The n_2 is directly related to the direct bandgap. For a-Si:H, the direct bandgap is smaller than c-Si; therefore the n_2 (real part of $\chi^{(3)}$) of a-Si:H becomes larger than c-Si. Typically for direct bandgap materials, α_2 will also increase with decreasing bandgap. However, for indirect bandgap materials such as silicon, the two photon absorption is more associated with the indirect bandgap. And according to the absorption measurement

by Shoji [19], the indirect bandgap is much greater than c-Si, so the α_2 will be smaller, resulting this high nonlinear FOM in a-Si:H.

Table 1.1: Nonlinear properties of different materials at $\lambda = 1550\,nm$

Material	n_2 (cm^2/W)	$Re(\gamma)$ $(1/W \cdot m)$	β_2 (cm/GW)	Nonlinear FOM
HNLF	3.2×10^{-16}	0.021		
As_2S_3 [20, 21]	3×10^{-14}	10	6.2×10^{-4}	High
c-Si [22]	4×10^{-14}	300	0.8	0.35
SiN [23]	2.5×10^{-15}	1.4	*Negligible*	High
Hydex [24]	1.1×10^{-15}	0.22	*Negligible*	High
GaAs	1.6×10^{-13}		15	0.07
AlGaAs (bandgap engineered) [25]	1.43×10^{-13}		0.05	13.2
a-Si:H (Suda *et al*) [26]	0.3×10^{-13}		0.2	0.97
a-Si:H (Narayanan *et al*) [27]	4.2×10^{-13}	2000	4.1	0.66
a-Si:H (Kuyken *et al*) [28]	1.3×10^{-13}	770	0.392	2.2
a-Si:H (Grillet *et al*) [29]	2.1×10^{-13}	1200	0.25	5
a-Si:H (Matres *et al*) [30]	1.7×10^{-13}	332	0.22	4.9
a-Si:H (Our device) [31]	5×10^{-13}	2000	1.43	2.25

Chapter 2

Wavelength conversion

2.1 Introduction

To fully utilize the wide bandwidth of optical communications, certain multiplexing schemes are widely applied. A typical scheme is called wavelength division multiplexing (WDM) where each user is allocated with a specific wavelength window. In this setting, the ability to transfer data from one wavelength to another becomes crucial for WDM implementation. Ultrafast nonlinear parametric process can be utilized for wavelength conversion. Here, we use pump-degenerate four-wave mixing (FWM) in a dispersion engineered a-Si:H waveguide to achieve ultra-broad bandwidth wavelength conversion. The high nonlinearity of the a-Si:H waveguide can reduce the power requirement for efficient operation and the limitations due to nonlinear loss will be discussed.

2.2 Continuous-wave (CW) wavelength conversion

For the continuous wave (CW) FWM experiment , two CW tunable laser sources are used to generate the pump and signal waves. The wavelength of the pump is fixed at 1541 nm and sent into an erbium-doped fiber amplifier (EDFA). The signal wavelength is swept from 1470 nm to 1540 nm. A wavelength-division multiplexer (WDM) is used to combine the pump and signal followed by a lensed fiber for fiber-to-chip coupling. The output light is collimated, coupled into a single mode fiber and sent into an optical spectrum analyzer (OSA).

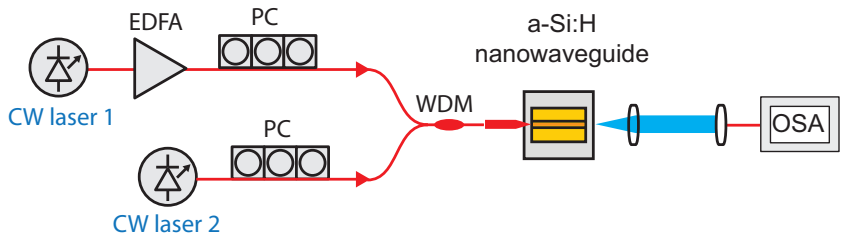

Figure 2.1: Schematic of experimental setup for CW four-wave mixing measurement.

The overlay of the wavelength-dependent FWM spectrum for the TE-mode is shown in Fig. 2.2(left) . The FWM occurs with -30 dB conversion efficiency over more than a 150 nm bandwidth, including the symmetric lobe to the short wavelength side, with only 2.2-mW of peak input pump power in the TE-mode. The full FWM bandwidth of the device has not been experimentally determined due to equipment limitations, however we expect it to be greater than 200 nm using the modeling method.

The measured and calculated conversion efficiency is plotted in Fig. 2.2(right) for the TE mode. The conversion efficiency is determined by $P_{idler\_out}/P_{signal\_out}$. The bandwidth modeling method is described in Sec. 2.4. We also measure and calculate the FWM conversion efficiency for the TM mode, and the conversion bandwidth of 20 nm is limited by the strong normal group-velocity dispersion value, as predicted by the modeling.

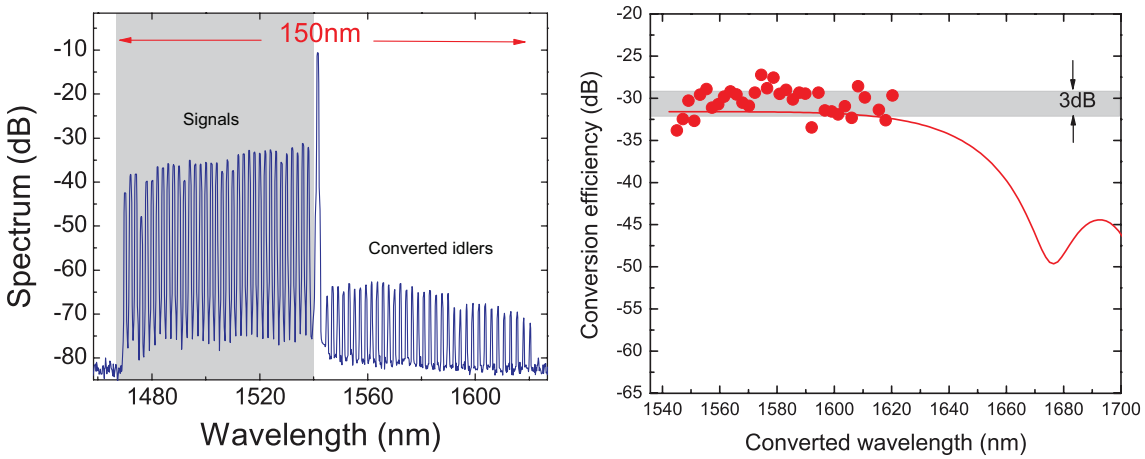

Figure 2.2: (Left)the overlay of wavelength dependent FWM when the pump is fixed at 1541 nm, and the signal is swept from 1470 nm to 1540 nm. (Right)Theoretical (curve) and experimental (dots) conversion efficiency as functions of converted wavelength for the TE-mode. A conversion efficiency of approximately -30 dB is measured over the 150 nm bandwidth including the symmetric lobe to the short wavelength side. The variation in conversion efficiency is in part due to the Fabry-Perot effects in the waveguide.

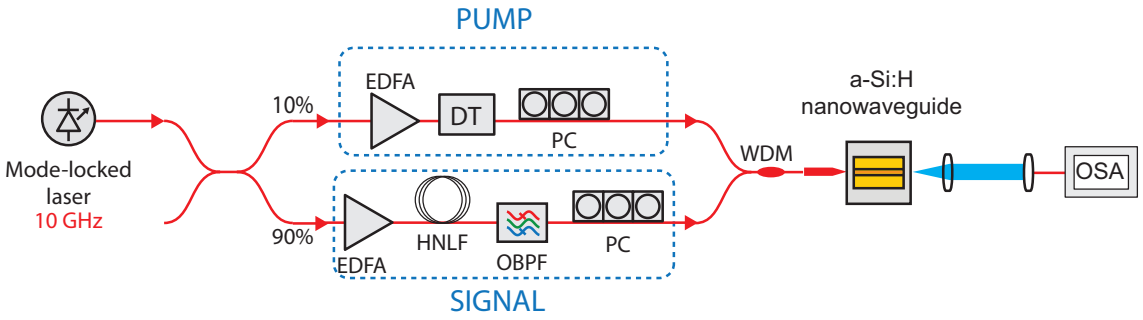

Figure 2.3: Telecommunication data rate (10 GHz) four wave mixing (FWM) experimental setup for a-Si:H waveguide.

2.3 Telecommunication data rate wavelength conversion

To demonstrate operation in the telecommunication regime, we carry out a pulsed FWM experiment using a 10 GHz repetition-rate source as shown in Fig. 2.3. The pump and signal pulses are produced using a 2.8 ps mode-locked fiber laser at 1560 nm with a 10 GHz repetition rate. After a 90/10 splitter, 10 % of the output is sent into a EDFA to amplify the pump pulses; 90% of the output is amplified and sent into highly nonlinear fiber (HNLF) to spectrally broaden the pulse followed by a tunable optical bandpass filter (OBPF) ranging from 1520 nm to 1600 nm for selection of the signal wavelength. An optical delay line is used to synchronize the signal and pump; and two polarization controllers are used to select the input guiding polarization modes. Signal and pump pulses are then combined using a WDM, and a lensed fiber is used for fiber-to-chip coupling. The light exiting the waveguide is collimated, filtered by a polarizer, and sent into an OSA.

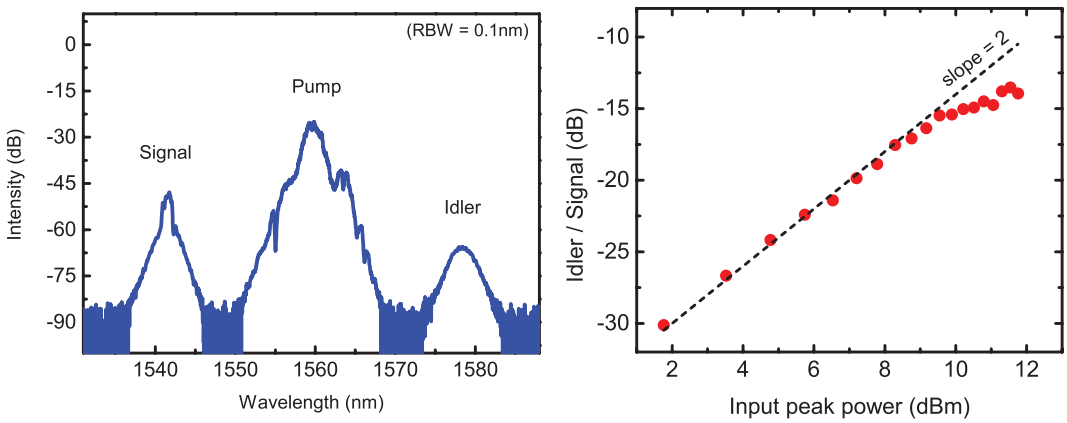

Figure 2.4: (Left) Sample 10-GHz four-wave mixing spectrum from a 8 mm a-Si:H waveguide when pump peak power is 8 mW. (Right) Maximum conversion efficiency as function of pump peak power. Dots represent the measured conversion efficiency and solid line shows the expected result from a quadratic relationship. Saturation due to nonlinear loss is observed when input power is greater than ∼10 dBm.

A sample FWM spectrum at 10 GHz with 8-mW input peak power is shown in Fig. 2.4 (left). The conversion efficiency is determined by the power difference between idler (pump on) and signal (pump off) both after exiting the waveguide. In our measurement, the maximum conversion efficiency is -13 dB; a value competitive with state-of-the art CW demonstrations in single crystal silicon (c-Si) [11] The comparison is valid when the free carrier lifetime is longer than the repetition rate. Through modeling, we estimate the difference in conversion efficiency between CW FWM and 10 GHz FWM to be less than 0.3 dB considering our ultralow peak pump power. The calculated power dependence of FWM conversion efficiency is shown in Fig. 2.4 (right) with the measured results (dotted). The saturation of the conversion efficiency at -13 dB is due to two-photon absorption-induced free carrier absorption loss. To model the power dependence of the conversion efficiency, we follow the analysis used

in [32]. The calculation agrees well with the measured conversion efficiency. As shown in Fig. 2.4, the conversion efficiency increases with increasing pump power, and then saturates at 10 dBm pump power.

2.4 Modeling the conversion efficiency

To model four-wave mixing effect wavelength conversion efficiency and bandwidth inside the silicon waveguides, we employ coupled mode equations that describe the pump, signal and idler wave propagating along the waveguide:

$$\begin{aligned}
\frac{dA_p}{dz} &= -\frac{1}{2}\left[\alpha_0^p + \alpha_2 I_p + \alpha_{FCA}^p I_p^2\right] A_p + i\gamma|A_p|^2 A_p \\
\frac{dA_s}{dz} &= -\frac{1}{2}\left[\alpha_0^s + 2\alpha_2 I_p + \alpha_{FCA}^s I_p^2\right] A_s + 2i\gamma|A_p|^2 A_s + \gamma A_p^2 A_i^* exp(i\Delta k z) \\
\frac{dA_i}{dz} &= -\frac{1}{2}\left[\alpha_0^i + 2\alpha_2 I_p + \alpha_{FCA}^i I_p^2\right] A_i + 2i\gamma|A_p|^2 A_i + \gamma A_p^2 A_s^* exp(i\Delta k z)
\end{aligned} \tag{2.1}$$

where I_p is the pump intensity; A_p, A_s, A_i are electric field for pump, signal, and idler; $\alpha_0^p, \alpha_0^s, \alpha_0^i$ are the linear propagation loss coefficients at pump, signal, and idler wavelength; α_2 is the two photon absorption coefficient; $\Delta k = 2\gamma|A_p|^2 - (2k_p - k_s - k_i)$ is the phase mismatch; k_p, k_s, k_i are wave vectors; γ is the effective nonlinearity of the waveguide; α_{FCA} is the free carrier absorption coefficient given by:

$$\alpha_{FCA} = \sigma_{FCA}\left(\frac{\lambda_p}{1.55\times 10^{-6}[m]}\right)^2\left(\frac{\alpha_2 \tau_{eff}\lambda_p}{2hc}\right) \tag{2.2}$$

where σ_{FCA} is the free carrier absorption cross section; τ_{eff} is the effective free carrier lifetime; h is Planck's constant.

By numerically solving these three differential equations, idler wave can be calculated. The simulation results are plotted along with the experimental data in Fig. 2.4 (right).

2.5 Conclusion

In this chapter, we demonstrate the nonlinear parametric process of four-wave mixing at continuous-wave and telecommunication data rate operation using an a-Si:H waveguide. The photonic waveguide is made from an a-Si:H film deposited at low-temperatures and can therefore be fabricated by standard CMOS technology at multiple stages throughout the fabrication process. The maximum FWM conversion efficiency at telecommunication data rates and wavelengths is competitive with state-of-the-art c-Si FWM demonstrations. However, this conversion efficiency is achieved with 10 dB less power due to the larger nonlinearity, suggesting its capability for nonlinear optical applications with extremely low power requirements. The conversion bandwidth can be controlled by dispersion engineering and is experimentally measured over 150 nm, or 20 THz, demonstrating the potential of a-Si:H for highly-integrated three-dimensional photonic-electronic networks.

Chapter 3

Optical time demultiplexing

3.1 Introduction

Optical time division multiplexing (OTDM) (Fig. 3.1) provides a spectrally efficient method for ultrahigh-bandwidth data transmission and has achieved performance beyond a terabaud (Tbaud) or one trillion symbols per second [33]. These ultrahigh data rates are well beyond the limitations of electronics and as a consequence require all-optical switching methods to manipulate the encoded information. In OTDM demultiplexing, lower rate channels (e.g. 10 Gbaud) are switched out individually from the ultrahigh rate signal (e.g. 1.28 Tbaud). (Fig. 3.2) As a result, full demultiplexing requires a large number of physical switches (e.g. 128 switches for 1.28 Tbaud to 10 Gbaud). Such all-optical processing systems are traditionally highly resource intensive in both size and operating power and therefore equipment

cost. For high-speed demultiplexing systems to be practical, the individual switches must become compact and operate at extremely low power levels.

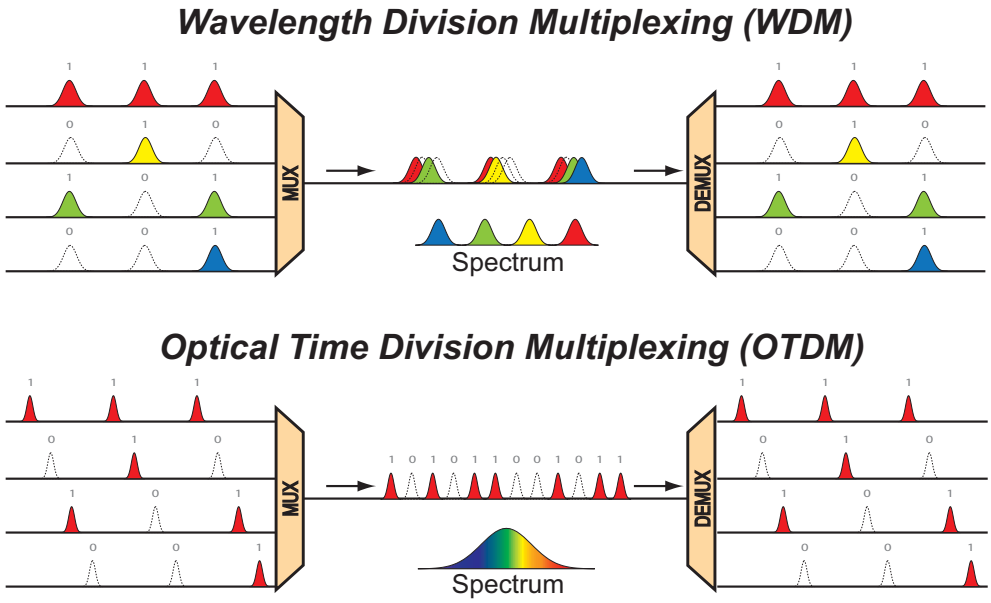

Figure 3.1: Schematic of WDM and OTDM. OTDM is a spectral efficient scheme. But the demultiplex requires ultrafast process that's beyond the limitation of electronics.

The extremely large effective nonlinearity indicates that comparable nonlinear efficiency can be achieved in a-Si:H nanowaveguides with greatly reduced power requirements in more compact devices.

Nonlinear photonic systems such as those required to demultiplex high-speed optical time-division multiplexed (OTDM) signals are typically extremely resource intensive in terms of size, power and cost. To minimize the resource requirements, integrated nonlinear photonic devices are highly attractive due to the potential for ultra-compact chip-scale systems and their high effective nonlinearity relative to fiber systems. Specifically, chalcogenide (As_2S_3) waveguides have been used to demulti-

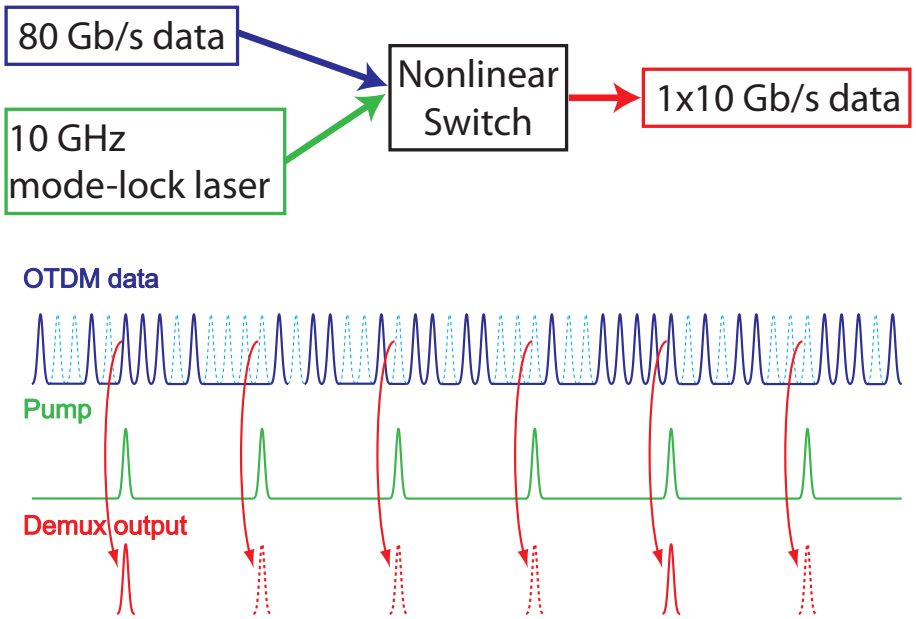

Figure 3.2: Schematic ultrafast nonlinear switch.

plex 1.28 Tb/s and 160 Gb/s data streams using peak optical control powers of 4 W and 4.4 W and waveguide lengths of 7 cm and 5 cm, respectively [34, 35]. Additionally, c-Si nanowaveguides were used to perform demultiplexing of 1.28 Tb/s and 160 Gb/s data streams to 10 Gb/s channels using peak powers of 2 W and 0.5 W and waveguide lengths of 5 mm and 1.1 cm, respectively [36, 37]. Semiconductor optical amplifiers (SOA) have been successfully used in demultiplexing [38] with low optical switching powers, but the device itself requires additional power for amplification. Using slow light photonic crystals, the enhancement of the nonlinearity can greatly reduce the length of the waveguide, but the power requirement is still relatively high (0.9 W) [39]. Silicon nano-crystals can achieve a very high nonlinearity ($n_2 > 10^{-12} cm^2/W$) and have been investigated in slot waveguide ge-

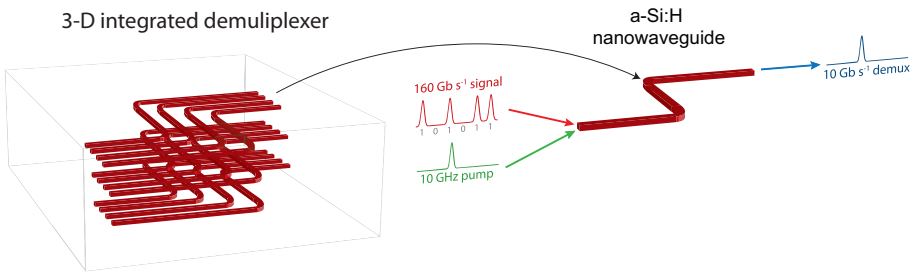

Figure 3.3: Hydrogenated amorphous silicon is a highly nonlinear material that can be deposited at low temperatures allowing for the creation of energy-efficient sophisticated three-dimensionally integrated ultrafast photonic processing circuits such as the demultiplexer depicted here.

ometries, however these structures typically exhibit much higher propagation losses (20 dB/cm) [40]. Lower switching energies have been achieved in photonic crystal resonant cavities [41] and ring structures [40], but the operating bandwidth is inherently limited due to the resonant cavity structure. An additional approach using a silicon-organic hybrid structure can potentially overcome the two photon absorption (TPA) induced free carrier absorption (FCA), but the high propagation loss and complex fabrication limit the device performance [42] and as a result, error free operation has not yet been demonstrated.

Here, we perform the first experimental investigation of demultiplexing high-speed optical time division multiplexed (OTDM) data signals in an a-Si:H nanowaveguide. Using four-wave mixing, we demonstrate demultiplexing of a 160-Gb/s OTDM data signal to 10-Gb/s with error-free performance for all 16 channels. Due to the ultra-high nonlinearity of the a-Si:H device investigated here, we are able to achieve error-free operation using ultra-low pump power. This power requirement is an order of

magnitude lower than previous CMOS-compatible integrated device demonstrations for OTDM demultiplexing. We also envision this efficient device can be applied to 3D integration and enables parallel demultiplexer within ultra-small device footprint (Fig. 3.3).

3.2 Experiment

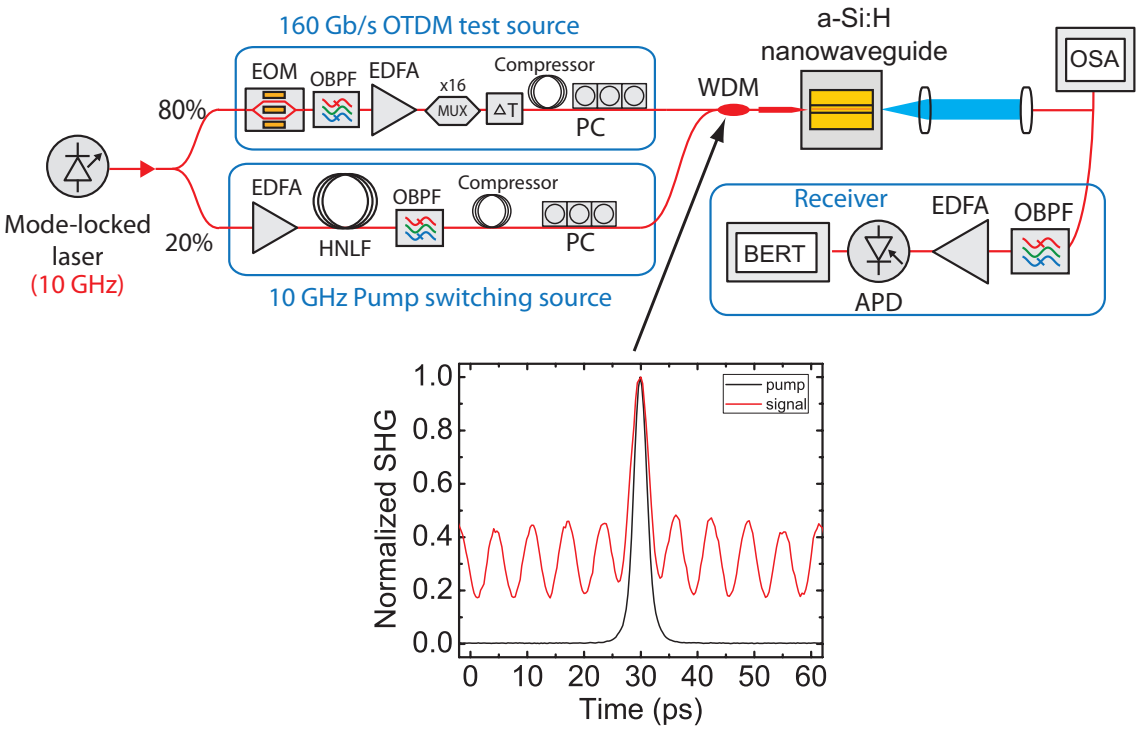

Figure 3.4: Experimental setup for 160-to-10 Gb/s all-optical demutiplexing using an a-Si:H waveguide (EOM: electro-optical modulator. TBPF: tunable bandpass filter. MUX: Mach-Zehnder multiplexer. PC: polarization controller. HNLF: highly nonlinear fiber. WDM: wavelength division multiplexer. PD: photo-detector. BERT: bit-error rate tester.). Inset: auto-correlation traces of 160-Gb/s signal and 10-GHz pump at the input of the waveguide.

We demonstrate OTDM demultiplexing from a 160 Gb/s on-off-keying (OOK)

data stream to 10 Gb/s with the a-Si:H nanowaveguide device using the experimental system shown in Fig. 3.4. An erbium-doped harmonically mode-locked fiber laser set to 1560 nm with a repetition rate of 10 GHz generates both the OTDM test source and the control pulses. An 80/20 coupler splits the test signal and pump sources, respectively. An electro-optic modulator (EOM) encodes the test signal with a 2^{31}-1 pseudorandom bit sequence (PRBS) and is then multiplexed up to 160 Gb/s using four highly asymmetric fiber Mach-Zehnder multiplexer (MUX) stages prior to being combined with the control pulses. The MUX stages are set to preserve a 2^9-1 PRBS sequence in the resulting OTDM signal. During the demux experiment, no change in the BER performance was observed when modulating at either 2^9-1 or 2^{31}-1 PRBS. The 20% side of the 80/20 coupler is spectrally broadened through self-phase modulation in 800 m of highly nonlinear fiber (HNLF) and subsequently filtered at a central wavelength of 1551 nm with a 4-nm bandwidth to generate the control pulses. A tunable delay (ΔT) and polarization controllers (PC) allow the test source and control pulses to be aligned in time and to be matched to the TE polarization of the waveguide. Compressing fibers are inserted at each arm to keep the control and test pulses transform-limited. The control and test sources are then combined using a wavelength division multiplexer (WDM). At the input of the waveguide, a lensed fiber is used for fiber-to-chip coupling. The waveguide output is sent into a receiver assembly, which consists of a 100-GHz optical filter centered at 1541 nm and optical amplifier followed by a second identical bandpass filter and an avalanche photo-

detector. The generated idler pulses are isolated and amplified prior to detection. The second bandpass filter is used to reduce the amplified spontaneous emission (ASE) from the amplifier. The detected signal is sent into a bit-error-rate tester (BERT) for error rate measurement. A 10% tap is implemented before the photo-detector for monitoring the received power during the BER measurement. During testing, an optical spectrum analyzer captures the spectrum before and after the waveguide. In the back-to-back (B2B) measurement, the mode-locked fiber laser is tuned to the idler wavelength (1541 nm), and the MUX stages are bypassed. These laser pulses are then sent directly into the receiver assembly of the experiment.

3.3 Results

The optical spectra before and after the waveguide are shown in Fig. 3.5(a). The data stream and pump laser are separated in wavelength by 10 nm. The average power for pump and signal inside the waveguide are 1.2 mW (0.8 dBm) and 0.8 mW (-0.9 dBm), respectively. The pulse widths of the pump and data pulses are measured through autocorrelation to be 1.9 ps and 2.1 ps (Inset of Fig. 3.4), respectively, corresponding to 63 mW peak power for the pump in the waveguide assuming a Gaussian shape pulse. At the output of the waveguide, the 160 Gb/s data is demultiplexed to 10 Gb/s at a wavelength of 1541 nm through FWM. The on/off conversion efficiency of the four-wave mixing process is measured to be -13 dB, a value competitive with

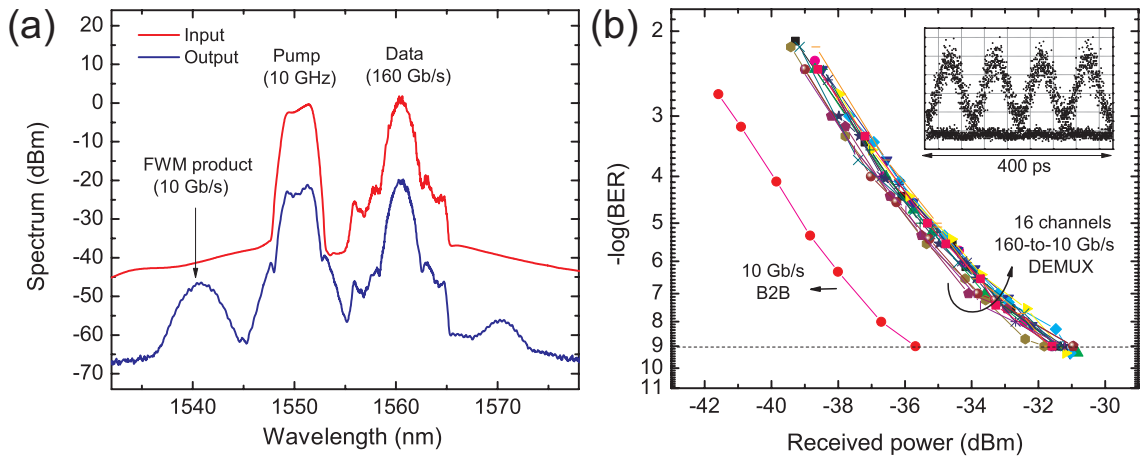

Figure 3.5: (a) Input and output spectra of the demultiplexing process in the 6-mm-long a-Si:H waveguide showing the input 160-Gb/s signal, the 10-GHz pump, and the generated 10 Gb/s idler. (b) The BER measurement of the 160 Gb/s to 10 Gb/s demultiplexing of all 16 channels and 10 Gb/s back-to-back (B2B). Error-free operation (10^{-9}) is achieved with 4- to 5-dB power penalty. Inset: demuxed eye diagram.

state-of-the-art demonstrations in c-Si. The on/off conversion efficiency is defined by the ratio between idler output power with the pump on and signal output power with the pump off, taking into account the duty cycle difference between the signal (160 Gb/s) and the idler (10 Gb/s) of 12 dB. The BER performance of this device for all 16 channels is shown in Fig. 3.5(b) demonstrating error-free operation with a BER of less than 10^{-9} and a power penalty ranging from 4 to 5 dB relative to the back-to-back (B2B) measurements. For reference, a demultiplexed eye diagram when the BER = 10^{-9} is shown in the inset of Fig. 3.5(b).

To study low power operation of the device, we investigate the minimum switching power necessary for error free demultiplexing (Fig. 3.6). While keeping the coupled OTDM signal power in the waveguide constant (0.8 mW average power), the pump

is attenuated to determine the minimum required switching power. As the pump is attenuated the conversion efficiency drops and the signal-to-noise ratio of the signal coupled out of the device suffers leading to increased error rate. Intriguingly, for this measurement error free operation is maintained with peak switching powers as low as 50 mW (17 dBm). This is an order of magnitude lower than previous CMOS-compatible integrated device demonstrations. Furthermore, with improvements to the output coupling efficiency of the waveguide (currently 8 dB) an even lower minimum switching power is possible.

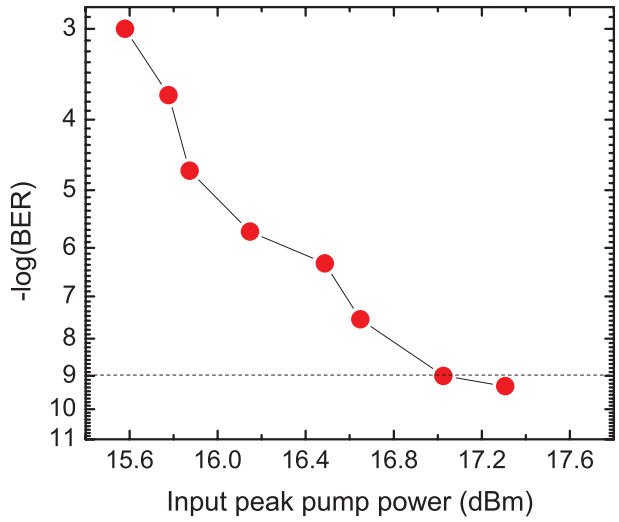

Figure 3.6: Bit-error rate as a function of coupled peak pump power. Error-free operation (10-9) is achieved with a 17-dBm (50 mW) peak switching power.

Table 3.1 compare our demonstration with previous approaches. Our results show that the power requirement for our device is at least an order of magnitude lower than the best c-Si demonstrations. Also, our device footprint is as small as 0.6 cm. Ultrafast efficient nonlinear switch can be achieve in a compact a-Si:H waveguide.

Table 3.1: OTDM demultiplexing using different platform

	Material	Data rate	Peak pump power	Device length
T. D. Vo *et al* [34]	As_2S_3	1.28 Tb/s	4 W	7 cm
M. D. Pelusi *et al* [35]	As_2S_3	160 Gb/s	4.4 W	5 cm
H. Ji *et al* [36]	c-Si	1.28 Tb/s	2 W	0.5 cm
F. Li *et al* [37]	c-Si	160 Gb/s	0.5 W	1.1 cm
This work	**a-Si:H**	**160 Gb/s**	**50 mW**	**0.6 cm**

3.4 Conclusion

Here we demonstrate 160 Gb/s to 10 Gb/s all-optical demultiplexing via four-wave mixing in a 6-mm long highly nonlinear hydrogenated amorphous silicon waveguide with error free operation at telecommunication wavelengths using ultralow peak pump powers of 50 mW. This represents the first demonstration of OTDM demultiplexing in a a-Si:H device and the switching power of our device is, to the best of our knowledge, the lowest among all CMOS-compatible platforms demonstrated to date. Excitingly, this material platform can also directly benefit from recent advancements in OTDM demultiplexing such as slow-light enhancement to further reduce the device size [39] and direct OTDM-to-WDM (wavelength division multiplexing) conversion to reduce the number of physical switches [43–45]. Furthermore, the low deposition temperature of the a-Si:H material used here allows such devices to be fabricated at

the back-end-of-the-line of a CMOS process, enabling their seamless integration with microelectronics. The demonstrated ability to manipulate ultrahigh data-rate signals using ultralow powers in a low temperature deposited waveguide offers exciting prospects for sophisticated multilayer on-chip all-optical signal processing circuits.

Chapter 4

All optical signal regeneration

4.1 Introduction

In optical communication links, signal degradation becomes a limiting factor in the maximum length and the data rate of the system. Amplifier noise known as amplified spontaneous emission (ASE), pulse dispersion, channel crosstalk, laser jitter, poor modulation, and nonlinear issues disrupt the definition between logical ones and logical zeros which leads to increased errors in the system. The contribution of these noise sources scales with the length of the communication link which ultimately limits either the bit error rate (BER) of the system or the length of the link. To overcome the signal degradation, signal regenerators are often employed in optical links. Optical-electrical-optical (O/E/O) repeaters commonly employed in optical networks for regeneration become expensive at high data rates and are limited in

speed. State of the art optical time division multiplexed (OTDM) signals have reached terabaud data rates [33] which is well beyond the limit of electronic devices. Along with ultra fast processing speeds based on kerr nonlinearity, all-optical processes offer the potential to perform regeneration on multiple channels simultaneously making all-optical signal regeneration indispensable to next generation communication systems [46].

Several optical regeneration methods have been proposed and demonstrated [47–51]. For return to zero on-off keying (RZ-OOK), the Mamyshev regenerator [50] can improve BER with two distinct power transfer functions for logical ones and logical zeros [51, 52]. The technique is based on nonlinear self-phase modulation (SPM) induced spectral broadening followed by a bandpass filter that has a center frequency offset from input central wavelength (Fig. 4.1). Since SPM spectral broadening scales with the temporal characteristics of the incident pulse power, energy from larger pulses will spectrally broaden into the offset filter range and energy from smaller pulses will not. For assumed logical zeros, the bandpass filter offset sets a threshold for input power so it can suppress low power noise sources that undergo little or no spectral broadening.. For logical ones, the method reduces amplitude fluctuations since larger pulses lead to energy spectrum broadening outside of the filter range. The output of the filter results in a transfer function resembling a step function where pulse power below a threshold has no output and pulses above a threshold have a constant level at the output. This is known as a 2R (re-shaping and re-amplification)

regeneration scheme (Fig. 4.2).

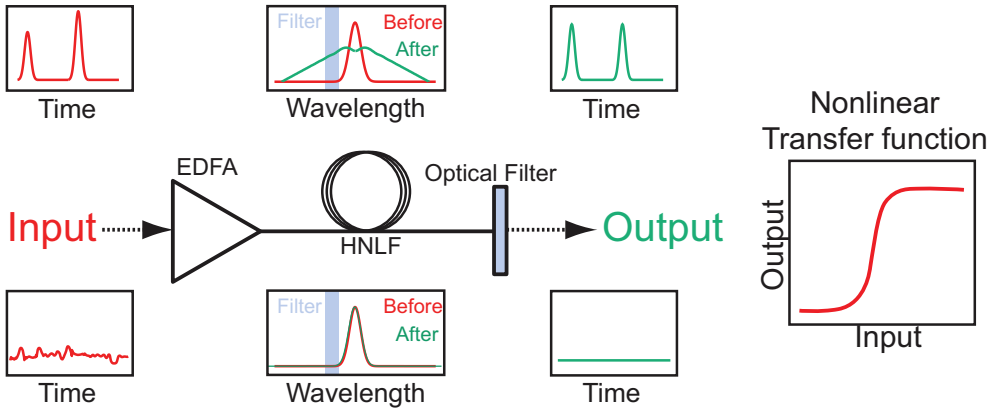

Figure 4.1: Schematic of Mamyshev 2R regeneration. Utilizing the self-phase modulation (SPM) in a highly nonlinear medium followed by an optical filter can reshape the degraded optical signals.

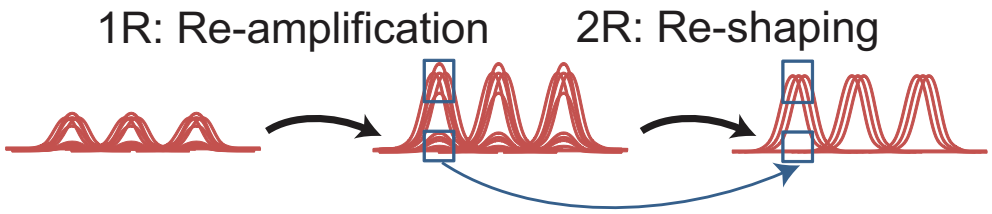

Figure 4.2: 2R regenerator re-amplify and re-shape the degraded optical pulses

The Mamyshev 2R regenerator has been shown at 40 Gb/s in 800 m of highly nonlinear fiber (HNLF) using peak powers of 1 W [51]. Much work has been placed into reducing the length of fiber required from regeneration devices. Utilizing material with higher nonlinearity can reduce the length requirement of the system. Chalcogenide (As_2S_3) fibers has been demonstrated at 9 MHz using 8W peak power with 2.8m fiber, but have yet to reach high data rates [51]. Integrated devices can further enhance nonlinearity from strong optical confinement inside the waveguide and

therefore reduce the length of the devices. Chalcogenide waveguides reduced size requirements to 22 cm, but this required an increase in the operating peak powers to 23 W and was only shown at 4 MHz [53]. Silicon waveguides allowed reduced power requirements (6W) while achieving even smaller sizes operating at 75 MHz although no BER improvement was demonstrated [54].

Here we demonstrate all-optical signal regeneration with BER improvement at telecommunication data rates using 10-mm-long highly nonlinear hydrogenated amorphous silicon waveguide.

4.2 Waveguide design and fabrication

For device design and modeling, the group veolicty dispersion (GVD) value for the TE mode of the designed waveguide (200 nm $\times$ 600 nm) is -500 ps/(nmkm). In SPM-broadened spectrum, normal group GVD can generate a flat-top shape and reduce the ripples in the transfer function of the regenerator [50, 55] making the negative GVD value of this waveguide an asset.

4.3 Experimental setup

The experimental setup for all optical regeneration in a-Si:H waveguide is shown in Fig. 4.3. A harmonically mode-locked erbium fiber laser at 1549 nm produces pulses at 10 GHz. An electro-optic modulator (EOM) encodes a pseudorandom bit sequence

(PRBS) onto the laser pulses. The EOM is modulated poorly to induce noise into the data stream. This simulates a degraded RZ-OOK format. A polarization controller is used to propagate the TE mode into the waveguide. An optical amplifier leading to the waveguide and an optical band-pass filter (OBPF) centered at 1547 nm following the waveguide make up the regeneration device for the incoming RZ-OOK data. A receiver composed of a 20 mW amplifier leading to an OBPF centered at 1547 nm and a 20 GHz photo-detector follows the regeneration device. The detected signal is sent into bit error rate tester (BERT) to measure the number of errors in the system.

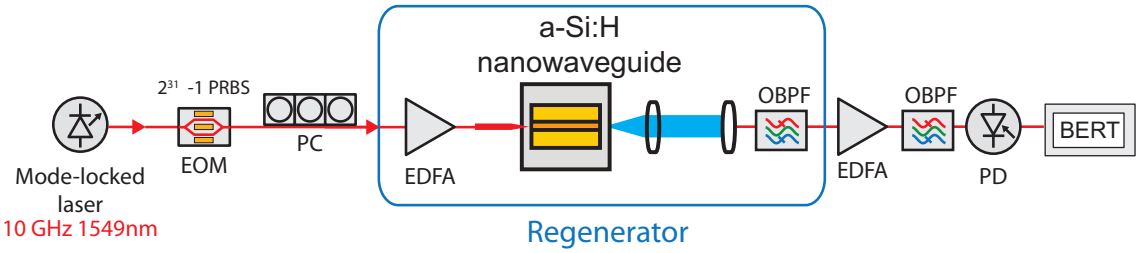

Figure 4.3: Experimental setup for 2R regeneration in a-Si:H waveguide.

4.4 Results

The optical spectrum of the a-Si:H waveguide is shown in Fig. 4.4(a). The SPM induced spectral broadening increases with the input power. Seven nanometers of broadening due to SPM can be obtained with pulses of 5.2 W peak power. The filter spectrum is also shown in Fig. 4.4(a), and has 100 GHz bandwidth with a 2 nm offset from the center of the input. When the input power is low (0.4 W), the SPM induced

broadening is too weak to reach the bandpass filter, which does not allow power in the output of the filter and results in logical zeros. When the input power is high enough (5.2 W or above), the energy from SPM broadens into the range of the filter and results in logical ones.

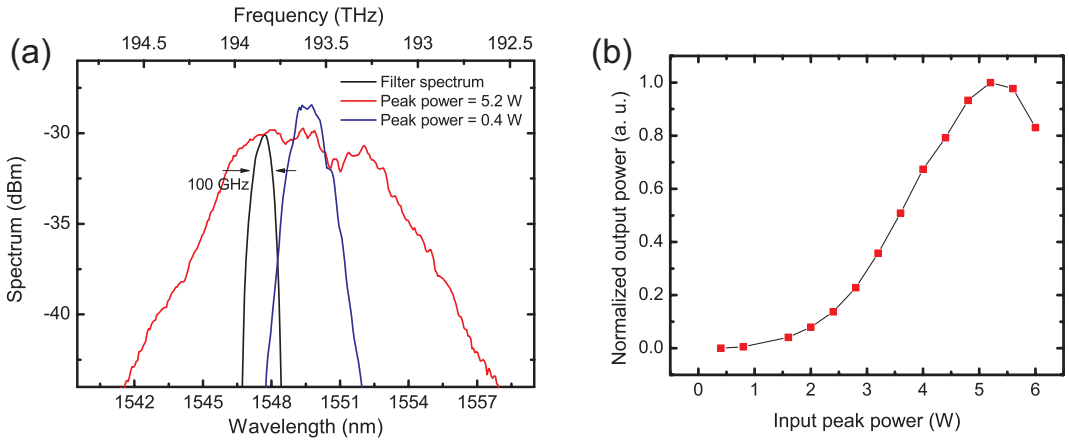

Figure 4.4: (a)SPM-broadened spectra of the a-Si:H waveguide when input peak power is 0.4 W and 5.2 W. The spectrum of the filter has 100GHz bandwidth. High power pulses will spectrally broaden into the filter range.(b)Measured power transfer function of the 2R regenerator. The output power saturates at 5 W.

The power transfer function is shown in Fig. 4.4(b). The transfer function shows S shape nonlinear curve of optical regenerators. The output has a quadratic response at low powers, and saturates at 5 W.

To evaluate the performance of the system, we compare the BER as function of power for the input and output of the regenerator. The power into the receiver is varied and the corresponding BER is measured. To measure the degraded signal at the input, the regenerator is bypassed and all of the filters are replaced with 100-GHz OBPFs at 1549 nm so the spectral center of the incident data stream is captured. As

seen in Fig. 4.5(a) , the regenerator takes a data stream with an error rate of 10^{-7} and improves it to error free transmission ($<10^{-9}$). The regenerator also acquires error free operation with power 2 dB less than the original signal showing a clear improvement of the signal quality. For a visual comparison, the eye diagram of the regenerated data stream the original signal at the same power level of -37 dBm are shown in Fig. 4.5(b). The corresponding histogram of the logical ones and logical zeros for input and regenerated signal are shown. It is clear from the histogram that the signal to noise ratio (SNR) is improved. The standard deviations of the histogram for the logical zeros and ones improve by 46% and 13% respectively. This corresponds to a SNR improvement of 1.5 dB which agrees with the measured BER from the BERT.

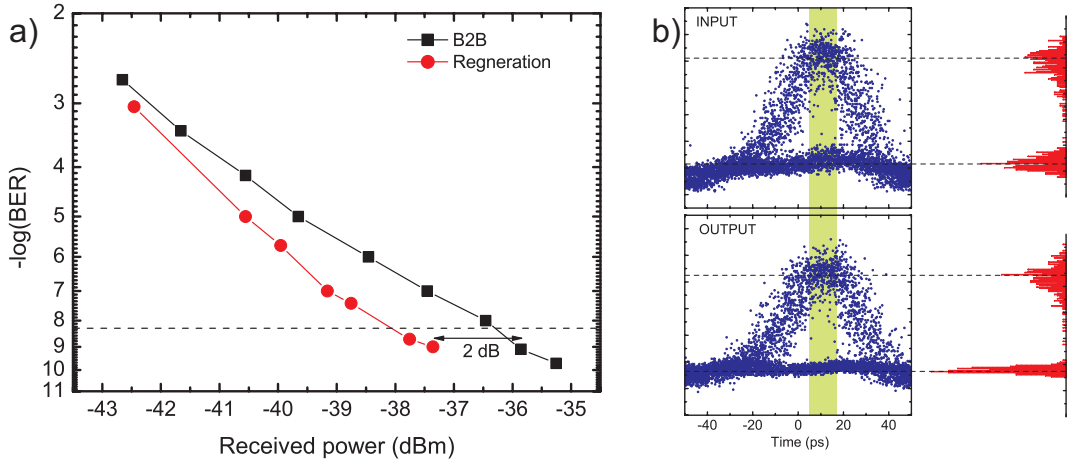

Figure 4.5: (a) The BER of regenerated signal and back-to-back (B2B) signal. The regenerated signal shows 2 dB received power improvement. (b) the eye diagram of input and output of the regenerator at same power level. The histograms show the samples in the shaded area which represents the distributions noise in logical ones and zeros

4.5 Discussion

We measure the original signal pulses in this system to be 1.5 ps and the regenerated pulses to be 6 ps. Based on the OBPF bandwidth, the regenerated pulses can be compressed to about 4.4 ps. Ideally, regeneration devices operate without pulse broadening. The broadening can be mitigated by utilizing a larger bandwidth OBPF. However, pulse width of 6 ps observed in the experiment is still much less than the standard 33% fill factor on 10 Gb/s signals indicating that the device can work for data rates up to 50 GHz without compression and 75 GHz with compression while utilizing the same OBPF bandwidth. The presented device is also applicable for regenerating signals demultiplexed from a high rate OTDM data stream, which often have output pulse widths narrower than required for the 33% fill factor. The small bandwidth allows better spectral efficiency when multiple channels from an OTDM signal are demultiplexed and combined in the same medium. Smaller bandwidths allows the device to operate on multiple channels in parallel. This is one of the key advantages of all-optical regenerators over O/E/O designs [46]. For data rates higher than 75 GHz, wider OBPF bandwidths are needed and may require higher power to induce enough spectral broadening.

4.6 Conclusion

We demonstrate a Mamyshev 2R all optical signal regeneration in a-Si:H waveguide operating at 5.2 W peak pulse powers yielding a received power improvement of 2 dB at 10 Gb/s data rates. To the best of our knowledge, this is the first demonstration of all optical signal regeneration in an a-Si:H platform and is the first demonstration to achieve telecommunication rates with BER improvement in integrated devices. Low operating powers, compact design, and three-dimensional integration capabilities show great potential for a-Si:H regenerators within on chip optical links.

Chapter 5

Short pulse characterization

5.1 Introduction

Future communications architectures such as optical time division multiplexing (OTDM) [33, 56–59], orthogonal OTDM [60], optical orthogonal frequency division multiplexing (optical OFDM) [61], and optical code division multiple access (OCDMA) [62] rely on ultrawide-bandwidth ultrafast sources such as mode-locked lasers and comb generators [63]. The performance of these systems relies heavily on the properties of the ultrafast source. As these systems shift to higher data rates, physical distortions such as dispersion and nonlinearities are magnified [33, 56–62]. Pulse characterization techniques are crucial for performance monitoring [64]; however, the ultrahigh-bandwidths required for these systems are difficult to measure by traditional means such as electronic and optical sampling [64–67]. Therefore ultrafast

self-referencing pulse characterization techniques such as frequency resolved optical gating (FROG) [68,69], modified interferometric field autocorrelation (MIFA) [70] and spectralinterferometry for direct electric-field reconstruction (SPIDER) [71] become indispensable to ultrafast laser characterization.

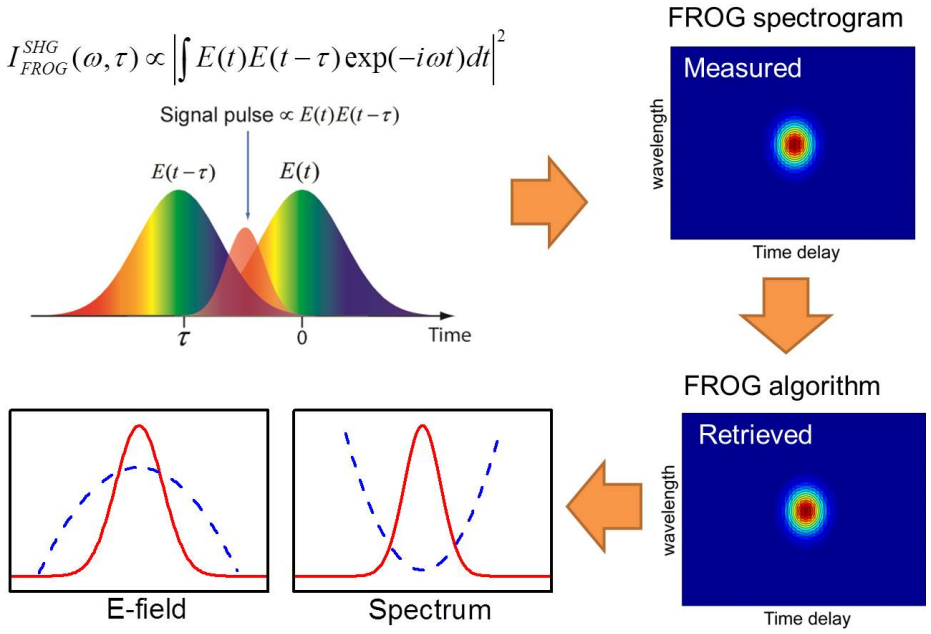

Figure 5.1: A time delayed replica of the pulse can gate out a portion of the original pulse. By saving the spectrum for different time delay can generate a spectrogram and an algorithm can calculate the amplitude as well as phase of the pulse.

Among these techniques, frequency resolved optical gating (FROG) is a highly effective and robust, self-referencing optical pulse characterization technique that fully characterizes an ultra-short optical pulse [68,69,72–75]. The concept of optical gating is described by Fig. 5.1. The most sensitive FROG geometry utilizes second-harmonic generation (SHG) between the pulse and a delayed version of the pulse. However, conventional free-space architectures used to exploit second-order nonlinearities have

difficulty measuring high repetition rate and low peak power pulses which are often found in high speed communications architectures [72–75]. To make FROG suitable for high repetition rate communications sources, architectures incorporating guided-wave nonlinear devices are being explored [76–81]. While impressive sensitivities ($2.7 \times 10^{-6} mW^2$) have been demonstrated in aperiodically-PPLN waveguides [78], this platform requires highly specialized materials thereby presents a challenge for efficient integration with telecommunications hardware. In comparison, the vast majority of guided wave devices do not exhibit a $\chi^{(2)}$ nonlinearity. For this reason a prominent guided-wave FROG architecture utilizes the $\chi^{(3)}$ nonlinear process of four-wave mixing (FWM) as a replacement to the SHG material. This facilitates the use of more abundant and relatively easier to manufactured materials such as highly nonlinear fibers (HNLF) [76], semiconductor optical amplifiers (SOA) [77] or c-Si waveguides [80]. Sensitivities ranging from 0.1 to 60 mW^2 have been demonstrated in these platforms.

Here in this chapter we investigate two FROG architectures using FWM in highly nonlinear hydrogenated amorphous silicon (a-Si:H) waveguides. Furthermore, the group-velocity dispersion (GVD) of these structures can be designed to allow for ultrawide-bandwidth operation. Due to the combination of high nonlinearity and wide-bandwidth operation, we demonstrate characterization pulses as short as 360 fs (with 2.5-THz bandwidth) with high sensitivity (6 mW^2) using the SHG-like FWM architecture. We expect the sensitivity can be improved to $<0.5\ mW^2$ by optimizing

the fiber-waveguide coupling. Secondly, we demonstrate a novel THG-like FROG architecture using two stages of FWM and demonstrate highly sensitive direction-of-time unambiguous FROG characterization of pulses as short as 1-ps with a sensitivity of $1 \times 10^6\, mW^2$. To the best of our knowledge, this THG-like FWM architecture is the first and most sensitive self-referenced guide-wave approach that overcomes the direction of time ambiguity of SHG FROG.

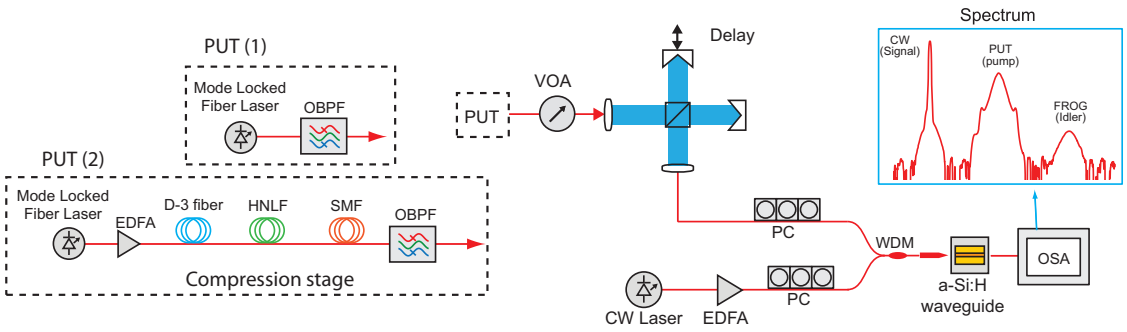

Figure 5.2: Schematic of experimental setup for SHG-like FWM-FROG measurement. Two different pulses under test are generated by a mode-locked fiber laser with or without the compression stage. Inset: optical spectrum at the output of the a-Si:H waveguide. (PUT: pulse under test. HNLF: highly nonlinear fiber. VOA: variable optical attenuator. WDM: wavelength division multiplexer. EDFA: erbium-doped fiber amplifier. OBPF: optical bandpass filter. PC: polarization controller. OSA: optical spectrum analyzer.)

5.2 SHG-like FWM-FROG

In this FWM architecture the pulse to be characterize is split, delayed, and recombined along with a CW laser [76, 77, 80]. Analogous to traditional bulk $\chi^{(2)}$ crystal SHG FROG approaches (Eq. 5.1), FWM architectures create the mixing of three

signals to generate a new signal at the idler frequency that resembles the traditional SHG FROG signal (Eq. 5.2).

$$E_{sig}(t,\tau) \propto E(t)E(t-\tau) \tag{5.1}$$

$$E_{idler} \propto E_{pump}(t)E_{pump}(t-\tau)E^{*}_{CW} \tag{5.2}$$

where E is the electric field to be characterized, E_{sig} is the developed FROG electric field, E_{pump} is the electric field to be characterized acting as a pump in the FWM stage, E_{CW} is the electric field component of the CW laser involved in FWM traditionally denoted as the signal, and E_{idler} is the developed electric field from the FWM process. Since the CW laser ideally does not exhibit ultrafast temporal characteristics this FWM generated signal is identical to the SHG FROG of the pulse to be characterized and can be extracted using standard SHG FROG algorithms after accounting for the offset center frequency. Utilizing this FWM technique, HNLF has yielded the best sensitivity of 0.1 mW^2 but was limited in signal pulsewidth to 7 ps due to the large interaction length required for such sensitivity [76]. To decrease the interaction length while maintaining similar sensitivities, semiconductor optical amplifiers and c-Si waveguides have demonstrated a sensitivity of about 50 mW^2 and 60 mW^2 respectively with pulsewidths around 3 ps [77, 80].

To test the sensitivity of the conventional SHG-like FWM-FROG in an a-Si:H waveguide (Fig. 5.2), a 10-GHz 1.8-ps pulse under test (PUT(1)) is split and combined using a free space Michelson interferometer with a variable delay arm. The fixed arm

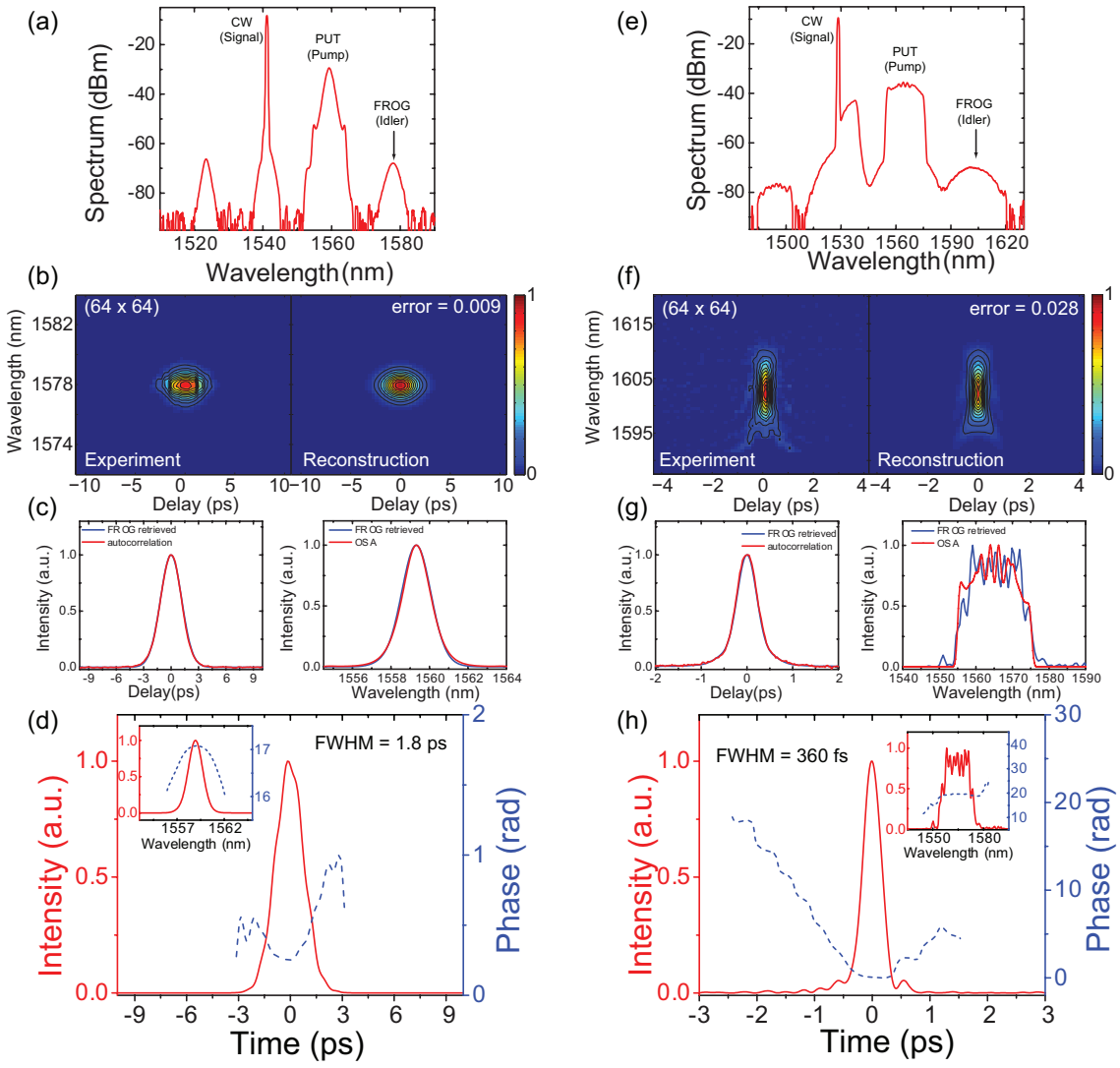

Figure 5.3: Pulse characterization of PUT 1 (left column), and PUT 2 (right column). (a),(e) Optical spectrum at the output of the waveguide. (b),(f) Measured and retrieved FROG. (c),(g) FROG retrieved auto-correlation and spectrum in comparison to the measurement. (d),(h) Retrieved amplitude and phase in both time and frequency domain.

is spatially dithered to avoid the interference fringes of the background [76]. The pulse and the delayed replica are coupled into the waveguide along with a CW laser using a lensed fiber. Polarization controllers are used in each path to match the TE

eigenmode of the waveguide and the pulses and CW probe undergo FWM. A typical output spectrum is plotted in the inset of Fig. 5.2. The FROG spectrogram is formed from the idler spectrum recorded using an optical spectrum analyzer (OSA) as the delay is varied. The results of this characterization are displayed in Fig. 5.3. The FWM spectrum is shown in Fig. 5.3(a). The measured and retrieved spectrograms of the 1.8-ps pulses are shown in Fig. 5.3(b). We obtain a retrieval error of <0.01 for the 64 x 64 grid. We compare the retrieved autocorrelation and spectrum with independently measured traces using an autocorrelator and OSA and find excellent agreement (Fig. 5.3 (c)). The retrieved intensity and phase in frequency and time domain is plotted in Fig. 5.3 (d). For this measurement, the input power to the FROG system is 900 μW. The retrieval error can be maintained below 0.015 while reducing the input power down to 320 μW, which corresponding to sensitivity of 6 mW^2. Furthermore, given that coupling losses to silicon waveguides of less than 3 dB have been demonstrated experimentally, we estimate that a sensitivity of better than 0.5 mW^2 is currently possible in this system.

To demonstrate the wide bandwidth capability of the waveguide, we characterize a 360-fs pulse with 20-nm (2.5 THz) bandwidth. A compression stage that comprises of dispersion shifted fiber, highly nonlinear fiber, and standard single-mode fiber is used to spectrally broaden and temporally compress the pulses from the 10-GHz laser (Fig. 5.2(PUT (2)). Fig. 5.3(e) shows the overall optical spectrum depicting the wide bandwidth of the pulses. The measured and the retrieved FROG trace of the 360-fs

pulse are plotted in Fig. 5.3(f) with retrieval error of 0.028. Independently measured auto-correlation and spectrum match well with the retrieved ones (Fig. 5.3(g)). The intensity and phase of the pulse are plotted in Fig. 5.3(h). Notably, this represents the shortest optical pulses characterized to date using the FWM-FROG architecture.

5.3 THG-like FWM-FROG

SHG FROG lacks the ability to distinguish absolute phase and the direction of high order phase changes which are included in PG and SD FROG geometries [68,69]. An alternative geometry based on third harmonic generation (THG) allows for a compromise between the high sensitivity of SHG FROG and the ability to define direction found in the other geometries. The free space versions of THG FROG are roughly identical to SHG FROG except a $\chi^{(3)}$ crystal is utilized [82–84]. This is difficult to develop in integrated and fiber platforms however, since phase-matching of the THG process is extremely challenging in guided wave structures and guided wave devices do not allow for spatial separation of the nonlinearly generated signals [68, 69, 82–84].

In communications settings, the direction of time of signal distortions is critical for performance monitoring. For example, characterization as fundamental as directly distinguishing between normal or anomalous GVD distortions is not possible with a simple SHG FROG measurement. Third harmonic generation FROG is one such

architecture that eliminates the ambiguity of time at the cost of sensitivity. In a very similar setup to free space SHG FROG, THG FROG combines a signal with a delayed replica of itself in a third order crystal to produce the third harmonic and a signal field represented in Eq. 5.3.

$$E_{sig}(t,\tau) \propto E(t)^2 E(t-\tau) \tag{5.3}$$

Since the third order process is less sensitive than second order processes, free space THG architectures are highly impractical for measuring telecommunications pulses. Here we demonstrate for the first time a FROG architecture using two stages of FWM to mimic a THG FROG measurement. A block diagram of the THG-like architecture is shown in Fig. 5.4.

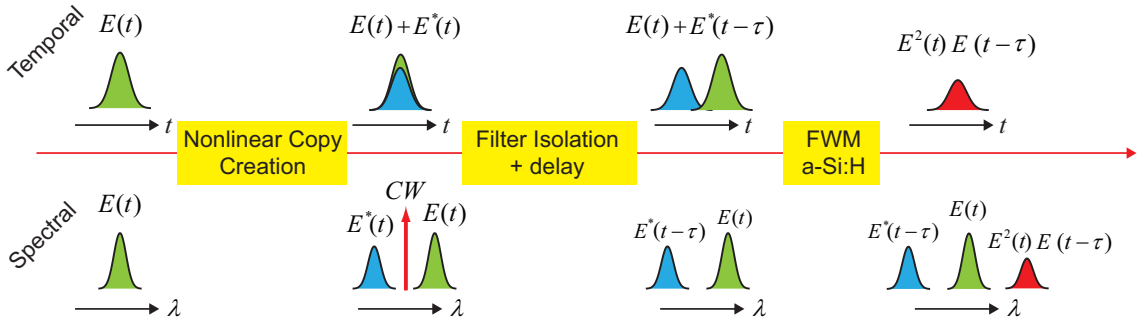

Figure 5.4: A block diagram of the cascaded FWM THG FROG. A nonlinear copy creation stage develop a replica of the pulse to be measured on a second wavelength. The two signals are isolated and delayed with respect to each other prior to mixing. The result from the mixing is read on a spectrum analyzer.

The pulse to be characterized is combined with CW laser prior to the first FWM stage. This initial FWM stage generates the complex conjugate of the pulse at a shifted wavelength. The CW source and higher order FWM content are removed using

spectral filters while the spectrally distinct conjugate and original pulse are separated. One pulse is delayed prior to recombining. The delayed pulse and conjugate mix in the second FWM stage to generate a signal at a new frequency that mimics a THG process (Eq. 5.4).

$$E_{idler}(t,\tau) \propto E_{pump}(t)^2 E_{conj}(t-\tau) \tag{5.4}$$

where E_{conj} is the replica of the signal to be characterized represented by E_{pump}. Finally, a standard THG FROG algorithm is applied to reconstruct the phase information of the pulse.

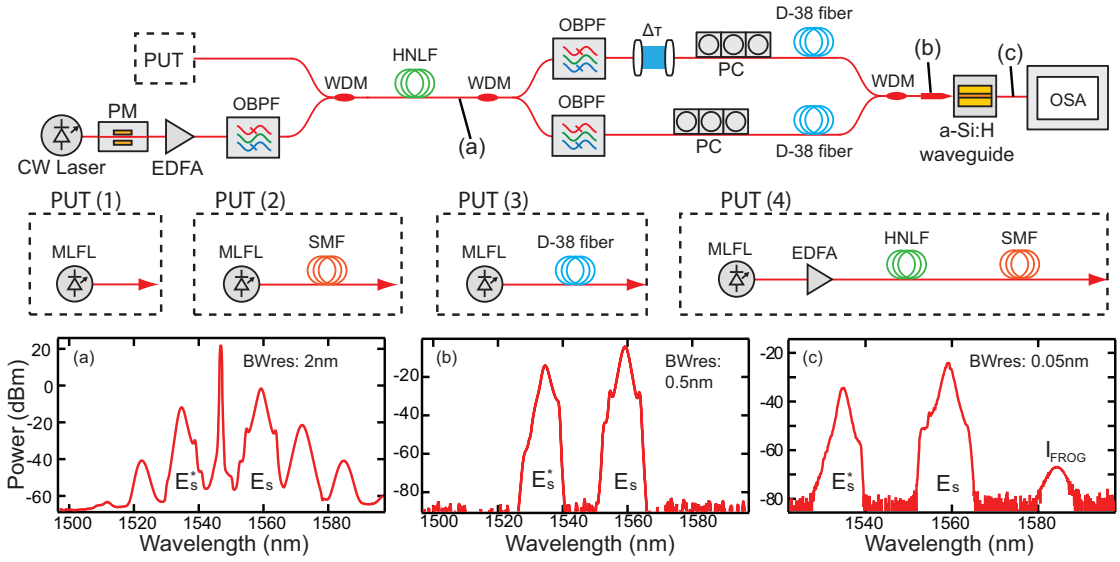

Figure 5.5: The experimental setup of cascaded FWM stages for THG FROG (PM: phase modulator. D-38 fiber: corning vascade S2000 fiber. MLFL: mode locked fiber laser). Insets (a), (b), and (c) show the spectrum of the experimental setup after the initial HNLF stage, before the waveguide, and after the waveguide respectively where BWres is the bandwidth resolution of the OSA.

The THG-like FWM FROG experimental system is shown in Fig. 5.5. A CW laser

is randomly phase modulated to mitigate stimulated Brillouin scattering (SBS) in the first FWM medium (HNLF), amplified to 2W by an erbium doped fiber amplifier (EDFA) and filtered by a 100-GHz filter centered at 1547 nm to provide a pump source for the first FWM stage. One hundred meters of HNLF is used for this stage to allow maximum conversion efficiency with minimal coupling loss. Since the CW pump is slowly varying, the frequency offset copy retains the complex conjugate of the phase information of the original signal [85, 86]. The typical spectrum developed from this process is shown in Fig. 5.5(a). A WDM isolates the conjugate pulse from the rest of the signals in the system which includes the CW pump, the original signal, and cascaded FWM effects and an additional WDM filter is used to fully suppress the CW pump energy that propagates through the first WDM. The conjugate pulse passes through a polarization controller (PC) and 3-m of dispersion compensating fiber to compensate for second and third-order dispersion of the PC and WDM filters. Another WDM combines the copy with the signal which propagates through its own PC, 4.5-m of dispersion compensating fiber, and a tunable delay. The combined signal and copy (Fig. 5.5(b)) are coupled into the 8-mm a-Si:H waveguide for the second FWM stage with greater bandwidth and sensitivity required to yield the THG-like FROG signal (Fig. 5.5(c)). As the signal is delayed relative to the conjugate pulse, the FWM idler spectrum is collected on an OSA to generate the FROG traces found in Fig. 5.6.

Figure 5.6 shows the FROG traces from four different test pulses: a 1.8-ps 10-GHz

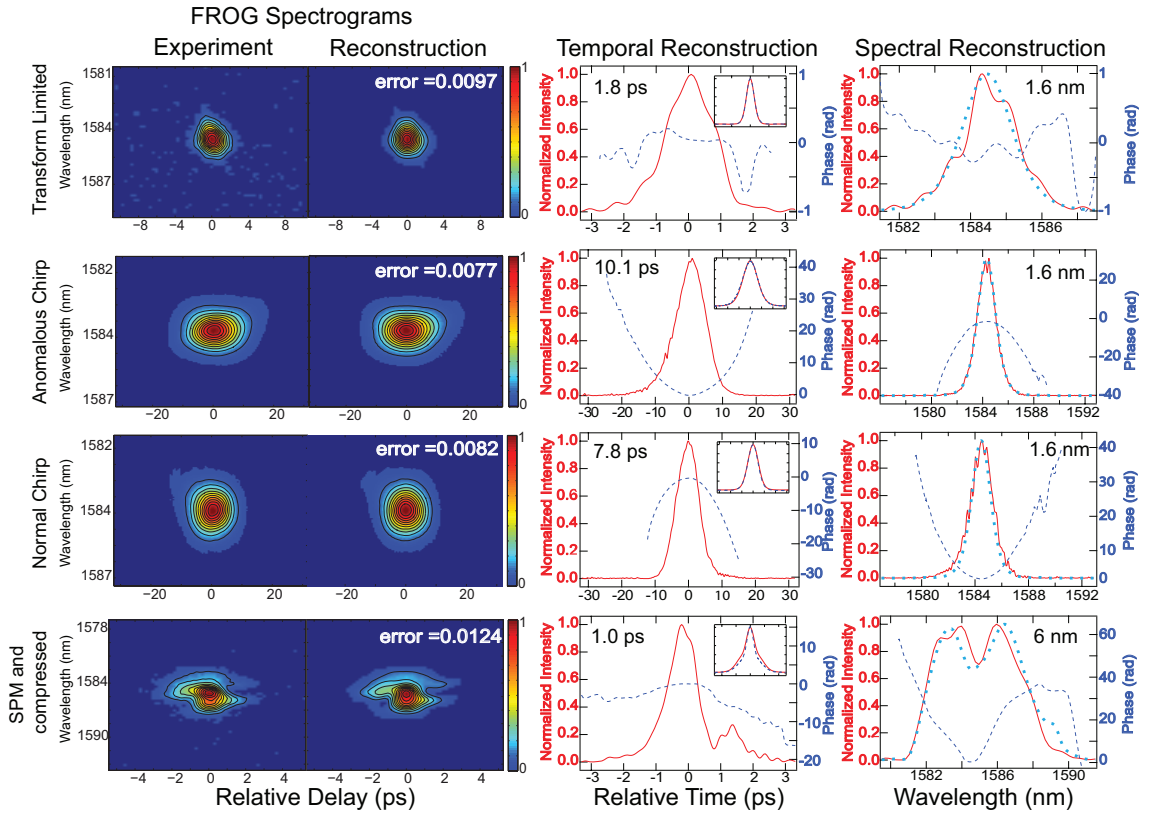

Figure 5.6: The experimental results where starting from left to right the columns show experimental FROG spectrogram traces, the reconstructed traces, the temporal reconstruction (solid) and its phase (dashed) with the corresponding experimental (dashed) and recovered (solid) autocorrelation in the inset, and the spectral reconstruction (solid) with its phase (dashed) and the measured spectrum (dotted) for the transform limited (top row), anomalously chirped (second row), normally chirped (third row), and self phase modulation with compression cases (bottom row).

harmonically mode-locked fiber laser (Fig. 5.5 (PUT 1)), the 1.8-ps pulse anomalously chirped to 10 ps in 350 meters of Corning single mode (SMF-28) fiber (Fig. 4 (PUT 2)), the 1.8-ps pulse normally chirped to 8 ps in 86 meters of Corning Vascade S2000 fiber (Fig. 5.5(PUT3)), and the mode-locked laser pulse spectrally broadened via a 250-mW EDFA in conjunction with 100 meters of HNLF, compressed in 5 meters of SMF-28 fiber. For the last case (Fig. 5.5(PUT 4)), 30 meters of HNLF is used for

the nonlinear copy creation stage to allow additional FWM bandwidth for the copy creation of a larger bandwidth signal. In each case, there is good agreement among the independent autocorrelations shown in the inset of the temporal reconstruction plots, and the spectral reconstruction develops the same bandwidth and overall shape as the independently measured spectrum. The details for grid size, error, pulse width, and spectral FWHM can be found in the respective plots.

The elimination of the direction of time ambiguity is clearly shown in the chirped cases. For the anomalous chirp, the temporal phase is concave up and the spectral phase is concave down. For the normal chirp, the phase distortions are reversed indicating that the pulse is chirped in the opposite direction. This is can also be seen directly in the respective FROG traces as the asymmetric wing in the upper right of the anomalously chirped trace which switches to the upper left in the normally chirped trace. In the SPM and compressed case, the temporal reconstruction has asymmetric ripples in the trailing wing of the pulse. Additionally, the V-shaped spectral phase includes a cubic response with the downturn in phase on the end of the spectrum. The combination of these two features and the temporal asymmetric ripple indicates that the pulse is predominately afflicted by SPM and third-order dispersion [69], as expected from the HNLF followed by SMF-28 fiber stages.

The transform limited trace is developed from a 7-mW average power 10-GHz pulse train illustrating the sensitivity of the device while acquiring a reconstruction error of less than 0.01. This measured sensitivity is $1 \times 10^6\ mW^3$ which is defined

as the peak power squared multiplied to the average power of the ultrafast laser input to this self-referenced system [87]. In the chirped cases, the average power is increased to 16 mW to acquire lower reconstruction errors. Further improvements to the sensitivity of this device may be acquired through mitigating splice losses and reduced coupling losses to the waveguide.

5.4 Conclusion

We demonstrate two FWM-based FROG architectures using a-Si:H waveguides which mimic SHG and THG FROG interactions. The a-Si:H waveguides have large nonlinearity and short interaction lengths with low dispersive properties allowing bandwidths of 2.5 THz and pulsewidths of 360 fs to be characterized with a sensitivity of 6 mW^2($<$0.5 mW^2 with improved coupling) which has comparable sensitivities to other FWM integrated methods [76, 77, 79, 80] while allowing for broader pulse bandwidths. The novel THG-like FWM FROG architecture allows self-referenced direction-of-time unambiguous ultrafast pulse characterization with sensitivities around 1×10^6 mW^3, pulse energies of 0.7 pJ for 10-GHz repetition rates. To the best of our knowledge, this architecture is the most sensitive self-referenced FROG technique that eliminates the direction-of-time ambiguity. Both of the architectures exhibit sensitivities suitable for next generation telecommunications signals.

Chapter 6

Optical parametric amplifier and oscillator

6.1 Introduction

CMOS-compatible on-chip optical amplification is a crucial building block for realizing on-chip optical networks. The use of c-Si, which exhibits a high linear and nonlinear refractive index and is compatible with current micro-fabrication technology, has resulted in a variety of exciting demonstrations including broad-bandwidth amplification using parametric processes [88] and oscillation utilizing the Raman effect [89]. However, in c-Si the net parametric amplification is limited by two photon absorption (TPA) and TPA-induced free carrier absorption (FCA) to be 5.2 dB at telecommunication wavelengths in pulsed experiments. Strong (50 dB) and broad-

band (37.5 THz) parametric amplification were obtained in the mid-infrared regime where TPA is avoided [90]; however, operating within this long-wavelength regime limits the applications for telecommunications. Exploiting the Raman effect has resulted in 13 dB amplification, but the crystalline nature of the material inherently limits the gain to a very narrow bandwidth (∼1 nm) [89]

Hydrogenated amorphous silicon (a-Si:H) has been shown to possess an extremely high optical nonlinearity with reduced impact of TPA, and parametric amplification as high as 26.5 dB has been achieved in pulsed experiments [28]. However, due to the relatively high group velocity dispersion (GVD) of the waveguide ∼1600 ps/(nm·km), the net amplification bandwidth was limited to ∼110 nm. Here, by carefully controlling the geometry of a hydrogenated amorphous silicon waveguide for near-zero GVD at the pump wavelength, we demonstrate optical amplification over more than 540 nm (66 THz). This represents the largest parametric gain bandwidth yet demonstrated in either c-Si or a-Si:H nanowaveguides.

6.2 Ultra-broad bandwidth a-Si:H optical parametric gain

The parametric amplification experimental setup is depicted in Fig. 6.1. A 90 MHz mode-locked fiber laser centered at 1558 nm is split with a 90/10 coupler. The pump pulse is generated by sending 90% of the laser into a 100 GHz optical filter followed by

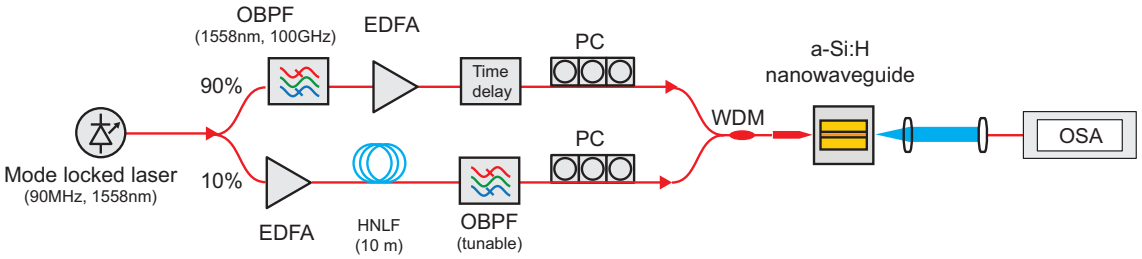

Figure 6.1: Experimental setup for the broad band parametric amplification measurement. (OBPF: optical bandpass filter. EDFA: erbium-doped fiber amplifier. HNLF: highly nonlinear fiber. PC: polarization controller. WDM: wavelength division multiplexer. OSA: optical spectrum analyzer)

an EDFA. The pump pulse width is measured by an autocorrelator to be 6.1 ps. The signal is generated by sending 10% of the mode-locked fiber laser into an EDFA and subsequently 10 m of highly nonlinear fiber to generate broad-bandwidth continuum. A free-space tunable filter is used to isolate the signal wavelength. A wavelength division multiplexer (WDM) combines the signal and pump arms for input into the chip. Fiber-to-chip coupling is achieved by a lensed fiber and lens collimator assembly. The lensed fiber input coupling loss is 8.5 dB; output lens-collimator coupling loss is 3 dB.

The optical spectra at the output of the waveguide are shown in Fig. 6.2(a). The red curve is recorded when the pump is turned off. When the pump is on, a clear amplification of the signal along with converted idler can be observed (blue curve). For this measurement the peak power of the pump is ∼3.6 W inside the waveguide. The amplification as function of wavelength is measured by tuning the signal wavelength and recording the respective pump on/off optical gain spectrum (Fig. 6.2(b)). With a pump wavelength of 1558 nm, a peak gain value of ∼16.7 dB is obtained for a

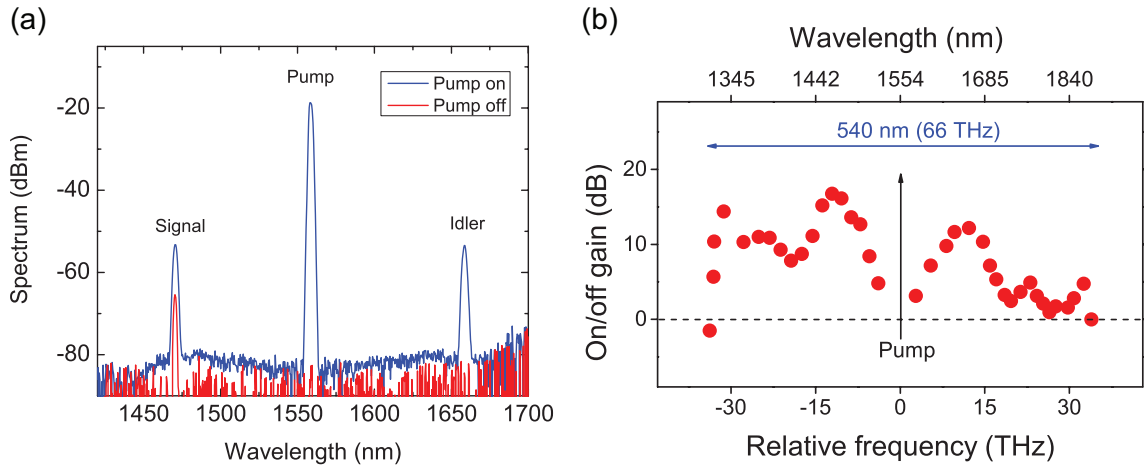

Figure 6.2: (a) Optical spectrum with pump on (blue) and pump off (red). (b) On/off gain as function of wavelength when pump is at 1558 nm.

signal at 1462 nm and the on/off gain bandwidth extends over more than 540 nm (66 THz). The gain at the longer wavelength lobe (>1765 nm, beyond the OSA limit) is measured by a home-made spectrometer. Table 6.1 summarizes all previous demonstrations and compares with this result. This demonstration represents the largest demonstrated on/off gain bandwidth of any c-Si or a-Si:H nanowaveguide demonstration.

Table 6.1: Optical gain bandwidth in various integrated demonstrations

	Mechanism	Material	Max gain	Gain bandwidth
Jalali [89]	Raman	c-Si	30 dB	1 nm
Kuyken [90] (Mid-IR)	Parametric amp	c-Si	>40 dB	580 nm (36.6 THz)
Foster [88]	Parametric amp	c-Si	5.2 dB	28 nm
Kuyken [28]	Parametric amp	a-Si:H	26.5 dB	64 nm
This work	**Parametric amp**	**a-Si:H**	**16 dB**	**540 nm (66 THz)**

6.3 A-Si:H GHz rate parametric gain

Using nonlinear parametric process and dispersion engineering, we have achieved 66 THz optical parametric amplification in a-Si:H. However, the optical amplification was operated in low repetition rate (∼MHz) to mitigate two-photon absorption induced free carrier effect. In order for optical amplifier to be useful in telecommunication applications, the ability of GHz operation is critical. Although using reverse biased p-i-n structure can sweep away the free carriers and CW Raman oscillation [91] can be achieved, the fabrication processes become complicated and no parametric amplification has been demonstrated with p-i-n structure [92].

In this section, we investigate a-Si:H OPA and utilize its high nonlinear FOM for GHz rate operation. Previously, we have demonstrated -13 dB conversion efficiency at 10 GHz and +16 dB conversion efficiency at 90 MHz. Here, we show that on-chip

amplification at 1 GHz can be achieved using this waveguide. This represents the first silicon-based OPA at telecommunications data rate.

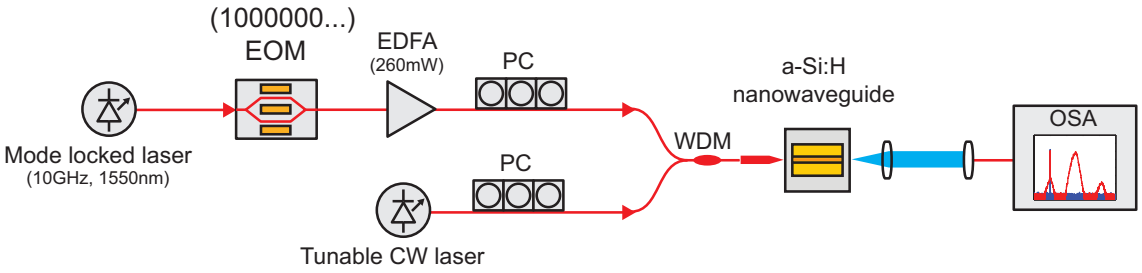

Figure 6.3: Schematic of experimental setup for 1-GHz optical parametric amplification measurement. (EOM: electro-optical modulator. WDM: wavelength division multiplexer. EDFA: erbium-doped fiber amplifier. PC: polarization controller. OSA: optical spectrum analyzer.)

The experimental setup for GHz rate OPA is depicted in Fig. 6.3. Pulses from a 10-GHz fiber mode-locked laser centered at 1550 nm are sent into an EOM (electro-optical modulator) that is encoded with an 1 and nine consecutive 0s to reduce the repetition rate. The pulses (pump) are then amplified by an EDFA and combined with a tunable continuous-wave (CW) laser (signal) using a wavelength division multiplexer (WDM). The pulse width of the pump is measured by auto-correlator to be ∼1.6 ps (assuming $sech^2$ shape) The pulsed pump and CW signal are coupled into the a-Si:H waveguide by a taper lensed fiber. Waveguide output coupling is achieved by lens-collimator assembly. The spectra are recorded by an optical spectrum analyzer (OSA).

The calculation of the on-chip signal gain and idler conversion is followed by Ref [93]:

$$Gain(signal) = \frac{P_{sig\_out}}{P_{sig\_in}} \cdot \frac{1}{Duty\ cycle} \tag{6.1}$$

$$Conversion(idler) = \frac{P_{idler\_out}}{P_{sig\_in}} \cdot \frac{1}{Duty\ cycle} \tag{6.2}$$

Figure 6.4 shows the measured gain and conversion with pump at different repetition rates. At higher repetition rates, the average power launching into the waveguide is higher and therefore limits the peak pump power we can inject before the damage threshold. It is clear that at around 1.35 GHz rate the signal gain exceed the transparency line and net on-chip gain is achieved. There is potential to achieve net gain at higher rep rate, but the high average input power is required. For the rest of this section, we will be focusing on the results of 1-GHz pump repetition rate.

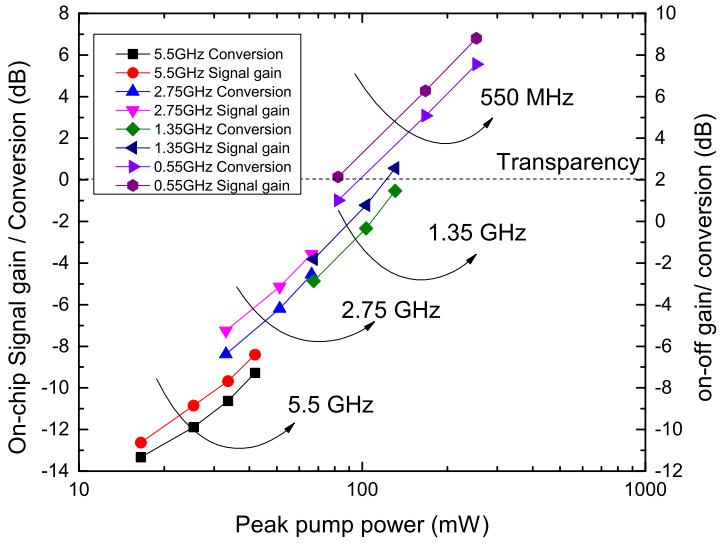

Figure 6.4: On-chip signal gain and idler conversion at different repetition rates.

Figure 6.5(a) shows the overlaid optical spectrum of the OPA with different signal wavelength (1480 nm∼1530 nm) when peak pump power is 630 mW (average power $\sim$ 1 mW). The wavelength dependent gain (and conversion) is plotted in Fig. 6.5(b). The OPA gain becomes stronger when the wavelength detuning is larger and the gain is expected to peak at ∼1462 nm [94]. We are not able to measure the gain/conversion with wavelength detuning >70nm due to our CW laser tuning range. We record the gain as function of pump power with a fixed signal wavelength (1510 nm). The results are plotted in Fig. 6.5(c). With hundreds of mW peak power (average power <1 mW) we can achieve on-chip gain. The gain can be as high as 10 dB and we see no gain saturation or sample degradation at this power level. With better fiber-to-chip coupling, we expect net off-chip gain can be obtained and GHz-rate optical parametric oscillator can be achieved.

In this section we demonstrate the first GHz silicon-based OPA using highly nonlinear a-Si:H waveguide. On-chip gain as high as 10 dB can be achieved with few hundreds mW peak pump power. This demonstration shows the potential for telecommunication optical amplifier and telecommunication data rate optical parametric oscillator (OPO) using this platform.

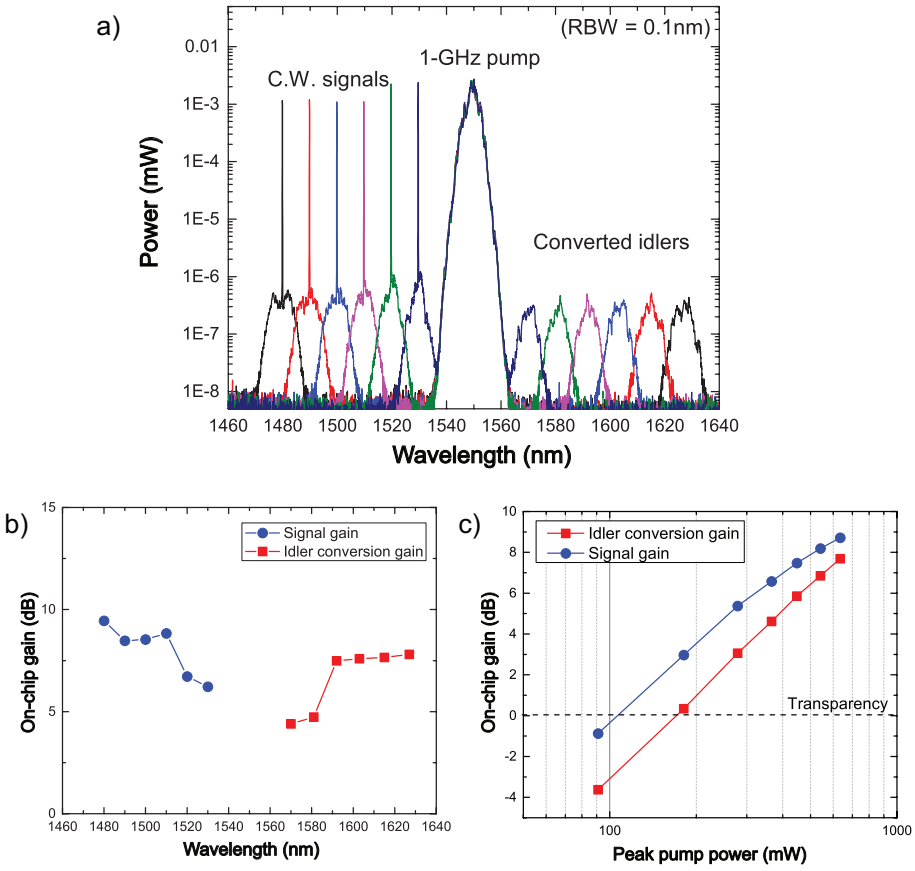

Figure 6.5: a) Measured optical spectra of optical parametric amplification for various signal wavelengths. b) On-chip gain/idler conversion as function of wavelength with pump at 1550 nm. c) On-chip gain/conversion as function of coupled peak pump power.

6.4 A-Si:H Optical parametric oscillator

A CMOS-compatible on-chip tunable light source is critically sought after in the field of silicon photonics. Raman oscillation has been demonstrated in c-Si but is severely limited in operating bandwidth (105 GHz) [3, 95]. In contrast, parametric optical processes can be designed to operate over extremely large bandwidths through geometric control of dispersion [11]. Pumping c-Si devices in the mid-IR has

allowed for demonstrations of large parametric gain [90, 93] and parametric oscillation [6]. However, at wavelengths near the telecommunications bands, the nonlinear performance of c-Si is severely limited due to two photon absorption (TPA) and TPA-induced free carrier absorption (FCA), allowing for parametric amplification of only a few dB [88]. Use of wider bandgap materials with negligible TPA (i.e. silicon nitride, or Hydex) has allowed on-chip multi-wavelength optical parametric oscillators (OPOs) [4,5] in near-IR, but the significantly weaker Kerr nonlinearity of these materials necessitates high optical powers and high-Q optical cavities to achieve oscillation. Figure 6.6 summarizes various approaches to realize silicon-based optical oscillator.

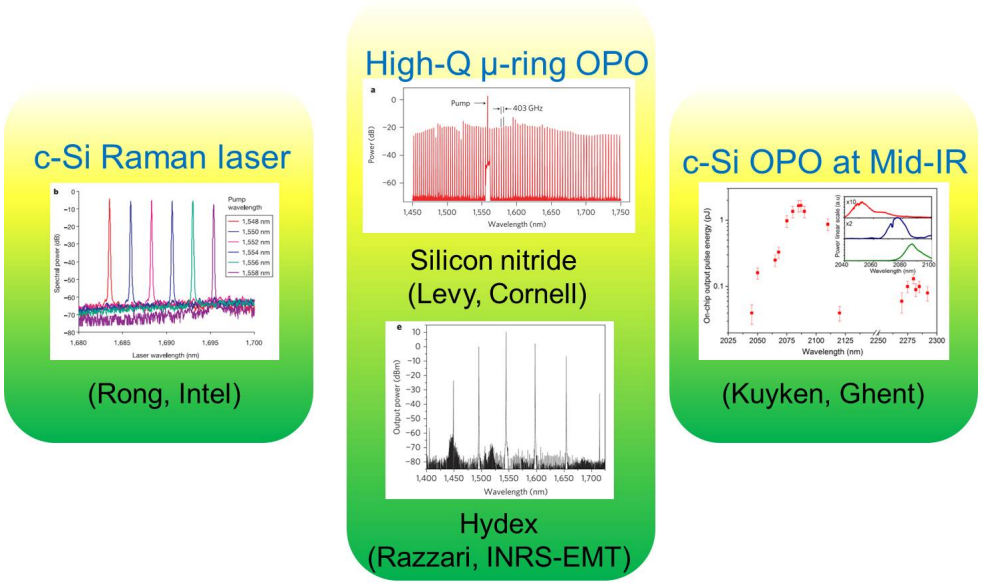

Figure 6.6: Approaches for achieving silicon-based optical light source [3–6].

Here, by utilizing the strong and broad bandwidth optical parametric gain and a fiber loop to build a widely tunable optical parametric oscillator. The dispersion

of the fiber allows simple time-dispersion tuning through modification of the cavity length and a tuning range of 42 THz (355 nm) is achieved.

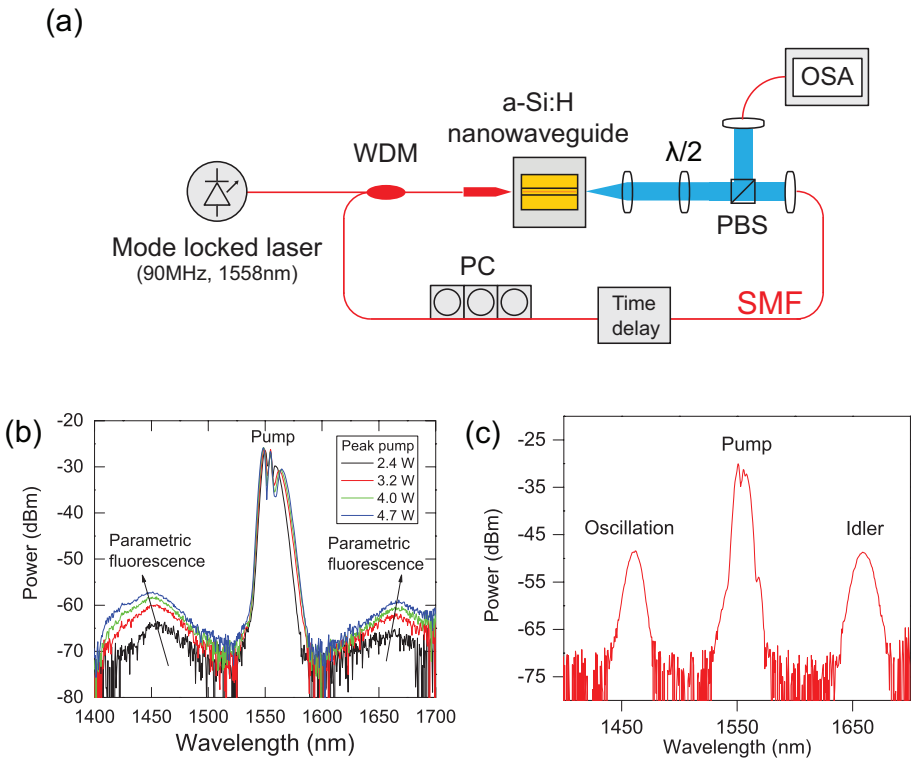

Figure 6.7: (a) Experimental setup for the optical parametric oscillator. (PC: polarization controller. WDM: wavelength division multiplexer. OSA: optical spectrum analyzer. PBS: polarization beam splitter. $\lambda/2$: half-wave plate. Red line: single mode fiber). (b) Single pass parametric fluorescence for different pump power. (c) Optical spectrum of the OPO when oscillation wavelength is at 1460 nm.

To harness the broadband parametric gain achieved in our a-Si:H waveguide, we place the device in a resonant-cavity to observe optical parametric oscillation. The experimental setup for oscillation is depicted in Fig. 6.7(a). A 90-MHz mode-locked fiber laser pump is centered at 1558 nm with a pulse width measured by auto-correlation to be 1.5 ps. Fiber-to-chip coupling is achieved by a lensed fiber and lens-collimator assembly with input coupling loss of 8.5 dB and an output lens-

collimator coupling loss is determined to be 3.5 dB. A half-wave plate and a polarization beam splitter are used to control the output coupling ratio of the fiber cavity. The length of the cavity created mostly from SMF-28 is chosen to match the repetition rate of the pump (2.3 m) and a polarization controller and free-space tunable delay are included in the cavity. The feedback light is combined with the pump using a wavelength division multiplexer (WDM). Figure 6.7(b) shows the spectrum for single pass parametric fluorescence without cavity. Once the single pass gain exceeds the round-trip loss, the cavity achieves oscillation. A sample oscillation trace is shown in Fig. 6.7(c) where the peak pump power in the waveguide is 2.5 W.

To determine the oscillation threshold of our device, the output of the oscillating mode (1470 nm in this case) as a function of input pump energy is plotted in Fig. 6.8(c), revealing the oscillation threshold to be 1.53 pJ with slope efficiency of $\sim$4.4%. The inset shows the evolution of the spectrum as the coupled pump energy increases. We measure the pulse width of this oscillation output through cross-correlation with a 1.5 ps reference pulse. The cross-correlation trace is shown in Fig. 6.8(d). The de-convolved pulse width of the oscillating mode is measured to be $\sim$1.1 ps.

As the majority of the cavity is built from single-mode fiber (SMF-28), the cavity exhibits net anomalous group-velocity dispersion, which allows for time-dispersion-tuning of wavelength by changing the physical cavity length of the OPO [96–99]. This tuning is achieved through control of the free-space delay in the cavity while the pump wavelength of 1558 nm remains fixed. We record the optical spectrum

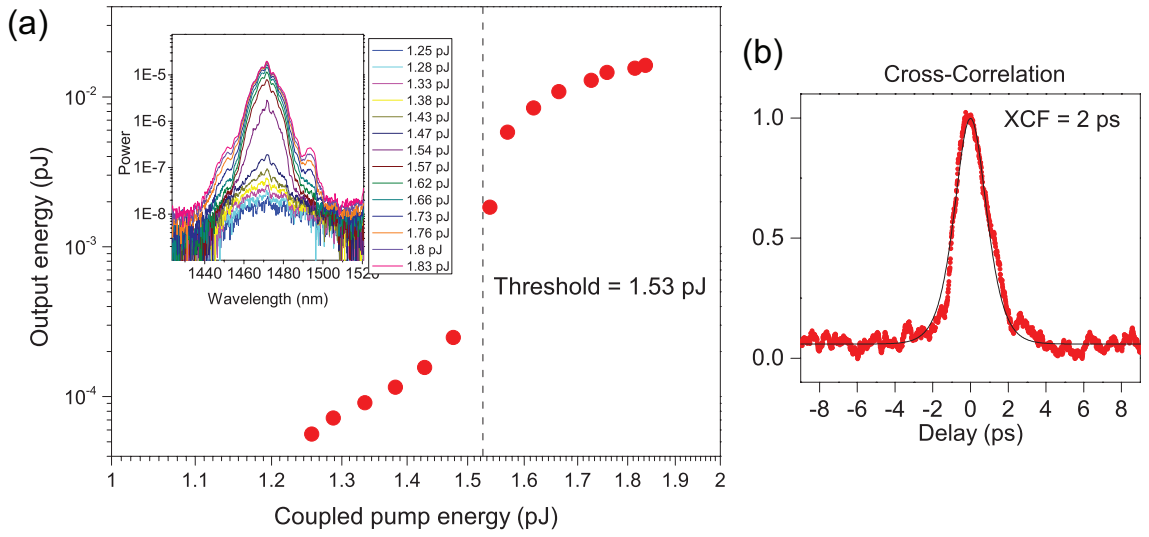

Figure 6.8: (a) Output energy of OPO as function of coupled pump energy. The oscillation threshold is 1.53 pJ with a slope efficiency of 4.4%. Inset: output spectrum as function of coupled pump energy. (b) Cross-correlation trace between oscillation (1476 nm) and a strong 1.5 ps pump. The de-convolved pulse width for oscillation output is 1.1ps.

of the oscillating mode for different cavity lengths and Fig. 6.9 shows the overlaid spectra from this measurement. We are able to tune the fundamental oscillating mode continuously from 1370 nm to 1515 nm, and 1600 nm to 1810 nm, corresponding to an overall wavelength tuning range of 42 THz (355 nm).

In this demonstration, the fundamental oscillating mode is limited to a maximum wavelength of 1810 nm, however through cascaded FWM, light can be generated at wavelengths outside of the parametric gain bandwidth. Figure 6.10(a) shows an example spectrum of the cascaded FWM process when the pump power is increased. When the oscillating wave (+1 mode) interacts with the pump and undergoes FWM, an idler is generated on the opposite side of the pump (-1 mode). These two waves mix with the pump wave to generate light at additional wavelengths (+2, -2, -3, -4 modes)

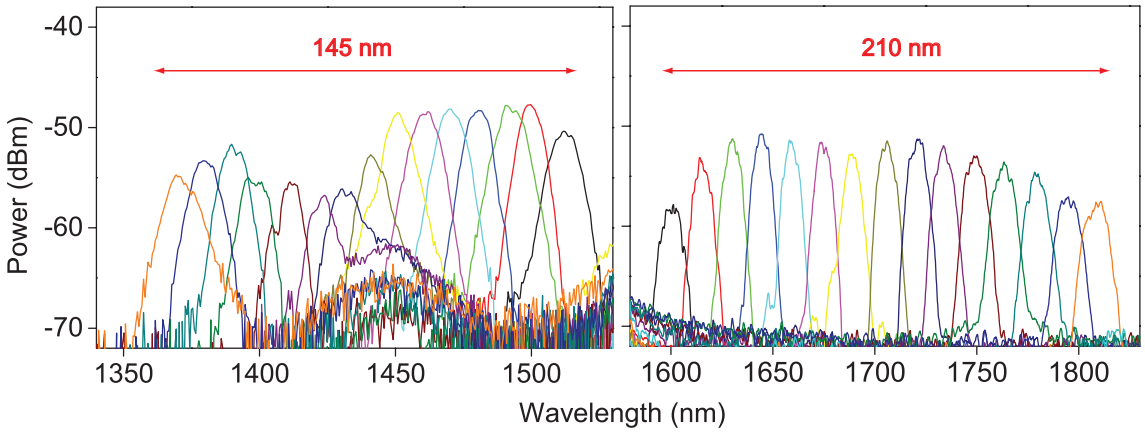

Figure 6.9: Overlaid tuning spectra of the oscillation mode at short wavelength side (1370 nm $\sim$ 1515 nm), and long wavelength side (1600 nm $\sim$1810 nm) for a 1558-nm pump laser.

through cascaded FWM. For wider separation of the oscillating mode from the pump, Fig. 6.10(b) shows the cascaded +2 mode generated at a wavelength of 1900 nm. We expect that by tailoring the dispersion of the waveguide, we expect the application can be used in the mid-IR regime, with potential spectroscopic applications in, for example, biological sensing and environmental monitoring.

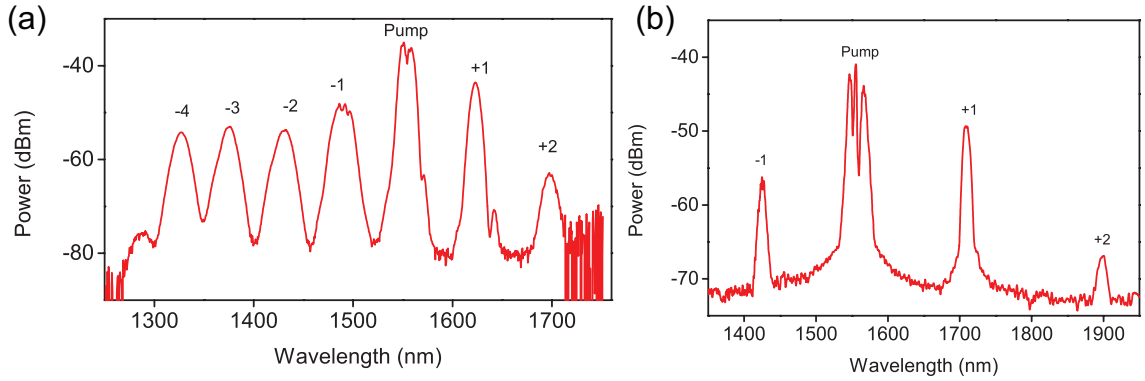

Figure 6.10: Wavelength extension through cascaded FWM. (a) Optical spectrum with increased pump power when +1 mode is on resonance. Cascaded FWM generates idlers at +2, -1, -2, -3, -4 modes. (b) Oscillating wavelength (+1 mode) near 1700 nm with cascaded FWM (+2 mode) for light generation at $\sim$1900 nm.

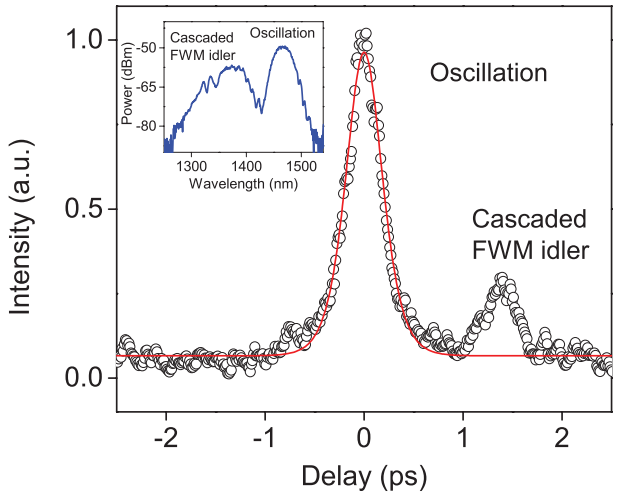

Figure 6.11: Cross-correlation trace of the oscillation mode (1467 nm) with a 250-fs reference pulse. The de-convolved pulse width for the oscillation mode is 300 fs assuming a $sech^2$ shape. The side peak in the trace is the cross-correlation of the cascaded FWM idler. (Inset: the output spectrum of the reduced net dispersion OPO cavity. The bandwidth of the oscillation mode is greater than 30 nm, allowing ultra-short pulse generation.)

As a final demonstration of the utility of this source, we demonstrate the potential for ultra-short pulse generation. The OPO cavity is modified to include both SMF-28 and dispersion compensating fiber (DCF) to minimize the net round trip dispersion. The oscillation wavelength is tuned to 1467 nm (inset of Fig. 6.11) and the bandwidth of the oscillation mode is greater than 30 nm. As shown in Fig. 6.11, we measure the pulse width of this oscillation output through cross-correlation with a 250-fs reference pulse. The de-convolved pulsewidth of the oscillating mode is measured to be 300 fs. Notably, the pulse width of the OPO pump laser is maintained at 1.5 ps for this demonstration. Furthermore, given the large parametric gain bandwidth of this device we anticipate that oscillating pulses well below 100 fs can be generated with improved cavity dispersion management.

In summary, we demonstrate the first deposited silicon optical parametric oscillator centered at telecommunications wavelengths. The broad bandwidth parametric gain enables wavelength tuning over the greater part of the extended telecommunications bands (E, S, C, L, and U) and beyond. This CMOS-compatible light source provides a robust near-infrared ultrafast wavelength-tunable light source that greatly extends the tuning range of ultrafast erbium-doped fiber lasers well beyond the C-band. Furthermore, the low oscillation threshold (1.53 pJ) and the high levels of parallelism made possible through multilayer CMOS device fabrication indicates that a vast multitude of synchronized wavelength-agile sources can be created using a single pump laser. Finally, we anticipate that the use of higher repetition rate pump lasers ($>$ 1 GHz) and hybrid integration with an ultralow-loss waveguide material (e.g. silicon nitride [100]) will provide a path towards integration of the full OPO cavity on chip.

Chapter 7

Correlated photon-pair generation

7.1 Introduction

Efficient CMOS-integratable quantum optical devices are highly desirable for implementing large-scale quantum information processing. Highly integrated active devices possessing strong optical nonlinearity, in particular, are essential for entanglement generation, optical logical operations, etc. Among a variety of candidates, silicon-based devices can already be mass-produced and integrated on a single chip using mature lithographic techniques. Thus far, compact sources of photon pairs have been developed in c-Si waveguides [101–103]. However, their applications in practice are restricted by virtue of strong two-photon absorption (TPA) and free carrier effects.

Previously Clemmen *et al.* reported a preliminary photon-pair generation experiment in an a-Si:H waveguide [104]; however, due to the relatively small γ (roughly

400 $W^{-1}m^{-1}$) and high linear loss of their waveguide (4.0 dB/cm), the photon pairs created were not of high quality, as assessed by low (< 10) coincidence-to-accidental ratio (CAR), much smaller than obtained in telecom fibers (~ 30) [105] and c-Si (> 50) [101].

In contrast, here we use our highly nonlinear a-Si:H waveguides to demonstrate efficient generation of high-quality photon pairs simultaneously in multiple spectral channels over a span of at least 5 THz. Using an 8-mm-long waveguide, we achieve CAR as high as 400 with pump peak power of around 10 mW. In addition, we quantify the contamination of photon-pair purity by spontaneous Raman scattering, and find it to be insignificant even at room temperature. Other background processes such as free-carrier effects are also suppressed due to the low pump power used. Our experiment spotlights a-Si:H as an ideal candidate for the next generation of highly integrable quantum optical devices, aided by its feasibility for creating complex, three-dimensional optical circuits on a chip.

7.2 Experiment

The experimental setup for generating multichannel photon pairs is depicted in Fig. 7.1. Light from a 50-MHz mode-locked femtosecond laser (IMRA CX-20) is filtered with two cascaded wavelength-division multiplexers (WDM) centered at 1555.8 nm, which together provide a (non-Gaussian) passing bandwidth of approximately

1 nm. A fiber polarization controller (FPC) and a fiber polarization beam splitter (FPBS) are followed to tune the input pump power to the waveguide. In order to ensure a constant input pump power over the duration of each measurement, the pump power is monitored in real time through a 90/10 power tap. Because the waveguide is optimized for FWM in the TE-like mode, another FPC is inserted before the waveguide to ensure correct polarization of the input pump. After the FPC, a lensed fiber is used for the fiber-to-waveguide coupling. A lens-collimator assembly collects the output light from the waveguide. A free-space polarizer is used in between the lens and the collimator to filter out any photons in the polarization state orthogonal to that of the pump. The total collection loss is measured to be 8 dB. The collected light is then passed through a free-space triple-pass grating filter (TGF) that rejects the pump with over 100 dB of isolation while selecting the spontaneous-FWM-created photons in two paired Stokes and anti-Stokes wavelength channels. By adjusting the geometry of the TGF setup, photons in different wavelength channels can be selected. For each channel, a (Gaussian like) bandwidth of 0.65 nm and a loss of approximately 2.6 dB are measured. The Stokes and anti-Stokes photons from each output port of the TGF are then detected, respectively, by single-photon counters with quantum efficiencies 2.7% and 1.9%. No pump photons are measurably present at the paired-channel detunings of 15 and 20 nm that we use in this experiment.

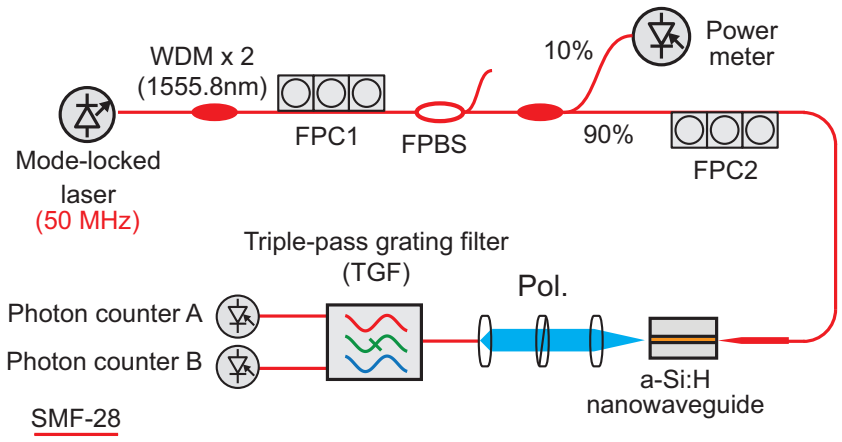

Figure 7.1: Experimental setup for photon-pair generation. (WDM: wavelength division multiplexer, FPC: fiber polarization controller, FPBS: fiber polarization beam splitter)

7.3 Results

In order to characterize the background Raman scattering, the single-photon counts after dark count subtraction in each channel for the 20 nm detuning are plotted in Fig. 7.2 as the pump power is varied. As described above, only photons co-polarized with the pump are collected through the filtering system into the single photon counters. Both the Stokes and anti-Stokes photon counts are plotted after being corrected for the respective total detection efficiency, which is attributed to the sub-unity quantum efficiencies of the detectors, and losses from the waveguide-fiber coupling, the polarizer, and the respective arm of the TGF. Here the total detection efficiency of each channel was calculated by relating the dark-count subtracted singles counts and the measured coincidence counts.

In the low-pumping regime ($\gamma P_0 L \ll 1$, where P_0 is the instantaneous pump power

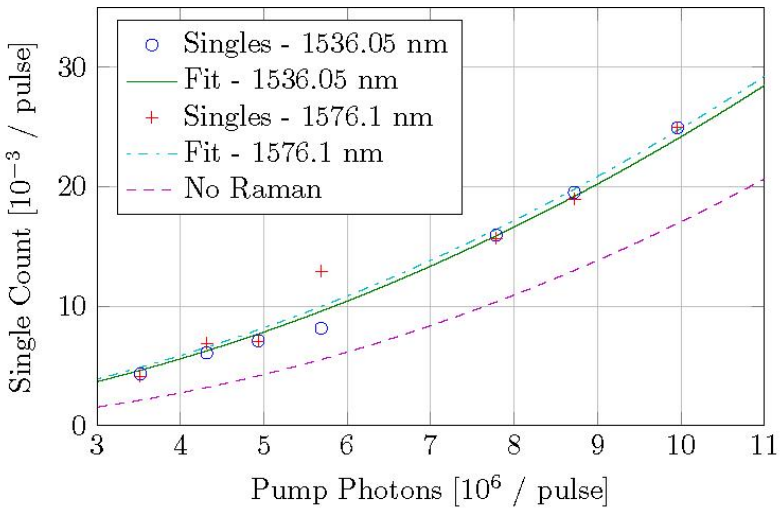

Figure 7.2: Singles counts per pump pulse as a function of pump photons for the case of 20 nm detuning. Both the Stokes and anti-Stokes data are shown along with their respective fits. Also shown is a per-pulse photon-number curve assuming no Raman scattering and only FWM. The statistical error bars for the experimental data are within the markers.

and L is the effective length of the waveguide), the number of photons generated by Raman scattering is linearly dependent upon the pump power while the number of photons generated through FWM is quadratic. Thus, in order to quantify the contribution of the Raman scattering, we fit our data using [106],

$$n_u = \Delta\nu_u \int (|\gamma P_0 L|^2 + P_0 L |g_R| N_u) d\tau \tag{7.1}$$

where the subscript $u = s$, a references the Stokes and anti-Stokes channels, respectively. n_u is the photon number per pulse, obtained by integrating the generated photon flux over the temporal duration of the pump pulse. $\Delta\nu_u$ is the filter bandwidth for each channel. ν is the phonon population given by the thermal distribution, with $N_a = n(\Omega)$ and $N_s = n(\Omega) + 1$ where, $n(\Omega) = [exp(\hbar|\Omega|/(k_B T)) - 1]^{-1}$, Ω is the

pump-Stokes frequency detuning, and T is the temperature of the waveguide. As discussed previously, γ of the present waveguide is known. This leaves the Raman gain coefficient, $|g_R|$, as the only free parameter in determining the production rate of the single photons as a function of the pump power. By using least-square fitting to the Stokes and anti-Stokes singles counts, good agreement is obtained between the fitting and the data, as shown in Fig. 7.2, giving a Raman-gain coefficient of $28 \pm 3W^{-1}m^{-1}$ ($38 \pm 3W^{-1}m^{-1}$) for the Stokes (anti-Stokes) channel for the detuning of 20 nm. Based on this result, even for low pump power, the photon-pair production dominates the Raman scattering at such a large detuning from the pump. For this experiment, at least 100 billion pump pulses are counted per pump power setting, with more than 500 billion pump pulses at the lower powers, for the purpose of reducing the statistical uncertainty. For a detuning of 15 nm from the pump, we similarly measure Raman-gain coefficients of $30 \pm 5W^{-1}m^{-1}$ and $45 \pm 8W^{-1}m^{-1}$ for the Stokes and anti-Stokes channels, respectively. The errors are larger in this case because of a change in the TGF efficiency and the detector dark counts over the course of these measurements.

The dark-count subtracted CAR measurement is plotted in Fig. 7.3. It is the ratio of the detector dark-count subtracted coincidence counts and the estimated accidental coincidence counts calculated from the product of the dark-count subtracted singles counts [107]. This procedure eliminates errors introduced into the accidental coincidence measurement by the detector dark counts, which are significant at low signal

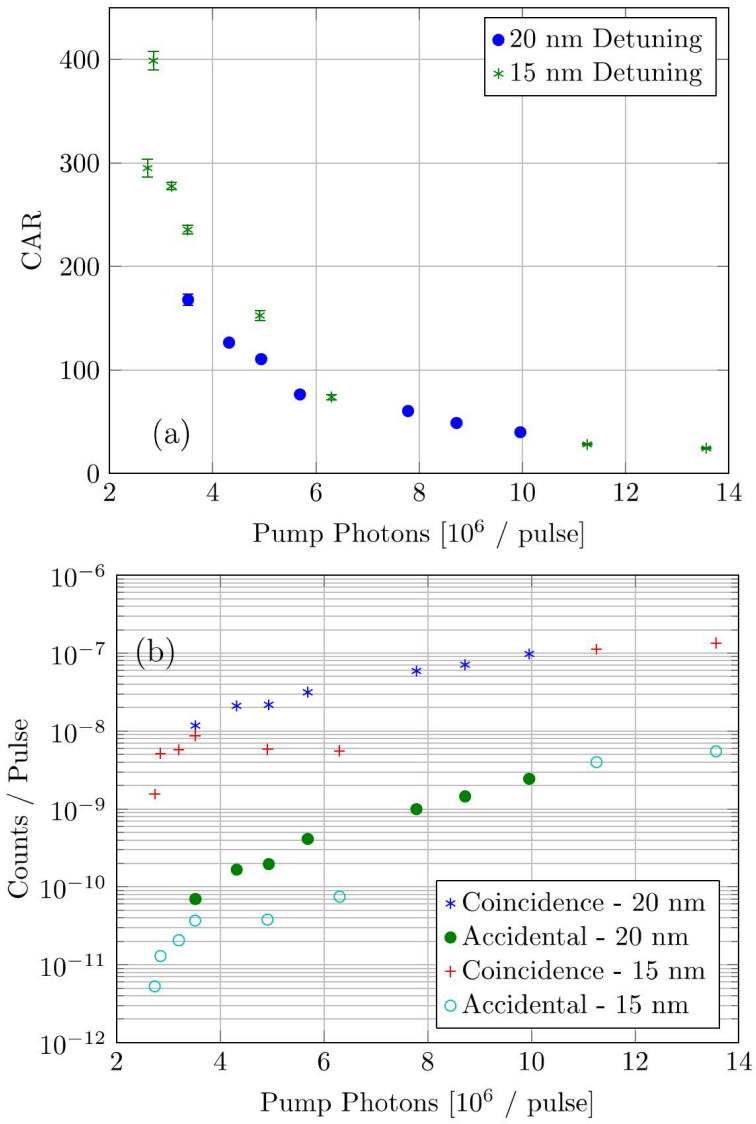

Figure 7.3: (a) Dark-count subtracted CAR versus the pump photon number per pulse. The highest CAR for the 15 nm (20 nm) detuning is 399 (168). (b) Dark-count subtracted coincidence and accidental coincidence count per pump pulse as a function of the peak pump power for both channels.

counts. Dark-count subtraction is accomplished by taking into account the accidental coincidences from the following sources: the probability of coincidences from true photon counts from one channel with dark counts from the other, and coincidences

of dark counts with dark counts from each channel. This procedure is necessary for the current detection system utilizing InGaAs avalanche photodiodes because of their inherent high dark-count level.

For a detuning of 15 nm, the maximum CAR recorded is near 400 for 2.8×10^6 pump photons per pulse, which corresponds to a photon-pair generation rate of 1.3×10^{-3} photons per pump pulse, whereas at a detuning of 20 nm, the peak CAR is close to 170 at a slightly stronger pump of 3.5×10^6 photons per pulse, corresponding to a per-pulse photon-pair generation rate of 2.2×10^{-3}. In contrast, the previous experiment using a similar waveguide with a CW pump measured CAR to be < 10 [104].

7.4 Discussion

The present CAR values are also much higher than those achieved in typical fiber sources, where small detunings ($< 4nm$) and liquid-nitrogen cooling are required to achieve the relatively high CAR values [13]. Also, the fact that high CAR values are obtained for a wide range of detunings showcases the wide bandwidth for photon-pair generation that can be engineered into these devices. Furthermore, the degrading effect of the larger Raman-gain coefficient relative to the c-Si devices, which results from the amorphous structure, is more than compensated by the extremely large optical nonlinearity, giving rise to the production of high-quality photon pairs.

We have demonstrated efficient photon-pair generation over multiple, widely detuned wavelength channels using a room-temperature a-Si:H waveguide. Our results suggest the advantage of such devices for future large-scale quantum optical applications, in terms of high efficiency, low background noise, and high CMOS-chip integrability. A potential application is near-deterministic generation of single photons via spectral and/or spatial multiplexing of heralded single-photon sources, whose low-power, on-chip realization is possible because of the extremely high nonlinearity of our waveguides.

Chapter 8

Conclusion and future work

8.1 Conclusion

Here I have investigated the optical nonlinear properties of this new silicon photonic material a-Si:H. The optical properties have been characterized by various measurement methods, and we have confirmed that a-Si:H has exceptional nonlinear properties that can be applied for ultra-fast optical parametric applications. I have also demonstrated various nonlinear applications, validating the use of this platform for low power all-optical signal processing.

8.2 Future work

We will continue to study the origin of the high nonlinear FOM of a-Si:H using time-resolved measurements and other advanced techniques. We will analyze the results by modeling the band-structure and derived the physics of the material. For the optical nonlinear applications, we will use this a-Si:H waveguide for super-continuum generation, phase-sensitive amplification, and ultimately, an integrated optical parametric oscillator on-chip.

Bibliography

[1] A. Alduino and M. Paniccia, "Interconnects: Wiring electronics with light," Nat Photon **1**, 153–155 (2007).

[2] N. Sherwood-Droz and M. Lipson, "Scalable 3D dense integration of photonics on bulk silicon," Opt. Express **19**, 17758–17765 (2011).

[3] H. Rong, R. Jones, A. Liu, O. Cohen, D. Hak, A. Fang, and M. Paniccia, "A continuous-wave Raman silicon laser," Nature **433**, 725 (2005).

[4] J. S. Levy, A. Gondarenko, M. A. Foster, A. C. Turner-Foster, A. L. Gaeta, and M. Lipson, "CMOS-compatible multiple-wavelength oscillator for on-chip optical interconnects," Nat Photon **4**, 37–40 (2010).

[5] L. Razzari, D. Duchesne, M. Ferrera, R. Morandotti, S. Chu, B. Little, and D. Moss, "Cmos-compatible integrated optical hyper-parametric oscillator," Nature Photonics **4**, 41–45 (2010).

[6] B. Kuyken, X. Liu, R. M. Osgood, R. Baets, G. Roelkens, and W. M. J. Green,

"A silicon-based widely tunable short-wave infrared optical parametric oscillator," Opt. Express **21**, 5931–5940 (2013).

[7] R. A. Soref, "Silicon-based optoelectronics," Proceedings of the IEEE **81**, 1687–1706 (1993).

[8] S. Assefa, "A 90nm CMOS Integrated Nano-Photonics Technology for 25Gbps WDM Optical Communications Applications," (2012).

[9] A. Harke, M. Krause, and J. Mueller, "Low-loss singlemode amorphous silicon waveguides," Electronics Letters **41**, 1377–1379 (2005).

[10] R. Takei, S. Manako, E. Omoda, Y. Sakakibara, M. Mori, and T. Kamei, "Sub-1 db/cm submicrometer-scale amorphous silicon waveguide for backend on-chip optical interconnect," Optics Express **22**, 4779–4788 (2014).

[11] M. A. Foster, A. C. Turner, R. Salem, M. Lipson, and A. L. Gaeta, "Broad-band continuous-wave parametric wavelength conversion in silicon nanowaveguides," Opt. Express **15**, 12949–12958 (2007).

[12] A. C. Turner, C. Manolatou, B. S. Schmidt, M. Lipson, M. A. Foster, J. E. Sharping, and A. L. Gaeta, "Tailored anomalous group-velocity dispersion in silicon channel waveguides," Opt. Express **14**, 4357–4362 (2006).

[13] V. R. Almeida, R. R. Panepucci, and M. Lipson, "Nanotaper for compact mode conversion," Optics Letters **28**, 1302–1304 (2003).

[14] B. Kuyken, H. Ji, S. Clemmen, S. K. Selvaraja, H. Hu, M. Pu, M. Galili, P. Jeppesen, G. Morthier, S. Massar, L. K. Oxenlø we, G. Roelkens, and R. Baets, "Nonlinear properties of and nonlinear processing in hydrogenated amorphous silicon waveguides," Opt. Express **19**, B146–B153 (2011).

[15] D. L. Staebler and C. R. Wronski, "Optically induced conductivity changes in discharge-produced hydrogenated amorphous silicon," Journal of Applied Physics **51**, 3262–3268 (1980).

[16] B. J. Eggleton, B. Luther-Davies, and K. Richardson, "Chalcogenide photonics," Nat Photon **5**, 141–148 (2011).

[17] J. S. Pelc, K. Rivoire, S. Vo, C. Santori, D. A. Fattal, and R. G. Beausoleil, "Picosecond all-optical switching in hydrogenated amorphous silicon microring resonators," Optics Express **22**, 3797–3810 (2014).

[18] D. J. Moss and R. Morandotti, "Platforms for integrated nonlinear optics compatible with silicon integrated circuits," ArXiv e-prints (2014).

[19] Y. Shoji, T. Ogasawara, T. Kamei, Y. Sakakibara, S. Suda, K. Kintaka, H. Kawashima, M. Okano, T. Hasama, H. Ishikawa, and M. Mori, "Ultrafast nonlinear effects in hydrogenated amorphous silicon wire waveguide," Optics Express **18**, 5668–5673 (2010).

[20] V. G. Ta'eed, M. R. E. Lamont, D. J. Moss, B. J. Eggleton, D.-Y. Choi, S. Mad-

den, and B. Luther-Davies, "All optical wavelength conversion via cross phase modulation in chalcogenide glass rib waveguides," Optics Express **14**, 11242–11247 (2006).

[21] M. R. Lamont, B. Luther-Davies, D.-Y. Choi, S. Madden, X. Gai, and B. J. Eggleton, "Net-gain from a parametric amplifier on a chalcogenide optical chip," Optics Express **16**, 20374–20381 (2008).

[22] M. Dinu, F. Quochi, and H. Garcia, "Third-order nonlinearities in silicon at telecom wavelengths," Applied Physics Letters **82**, 2954 (2003).

[23] K. Ikeda, R. E. Saperstein, N. Alic, and Y. Fainman, "Thermal and Kerr nonlinear properties of plasma-deposited silicon nitride/ silicon dioxide waveguides," Opt. Express **16**, 12987–12994 (2008).

[24] D. Duchesne, M. Ferrera, L. Razzari, R. Morandotti, B. E. Little, S. T. Chu, and D. J. Moss, "Efficient self-phase modulation in low loss, high index doped silica glass integrated waveguides," Optics Express **17**, 1865–1870 (2009).

[25] J. S. Aitchison, D. C. Hutchings, J. U. Kang, G. I. Stegeman, and A. Villeneuve, "The nonlinear optical properties of AlGaAs at the half band gap," Quantum Electronics, IEEE Journal of **33**, 341–348 (1997).

[26] S. Suda, K. Tanizawa, Y. Sakakibara, T. Kamei, K. Nakanishi, E. Itoga, T. Ogasawara, R. Takei, H. Kawashima, S. Namiki, M. Mori, T. Hasama, and

H. Ishikawa, "Pattern-effect-free all-optical wavelength conversion using a hydrogenated amorphous silicon waveguide with ultra-fast carrier decay," Optics Letters **37**, 1382–1384 (2012).

[27] K. Narayanan and S. F. Preble, "Optical nonlinearities in hydrogenated-amorphous silicon waveguides," Optics Express **18**, 8998–9005 (2010).

[28] B. Kuyken, S. Clemmen, S. K. Selvaraja, W. Bogaerts, D. Van Thourhout, P. Emplit, S. Massar, G. Roelkens, and R. Baets, "On-chip parametric amplification with 26.5dB gain at telecommunication wavelengths using CMOS-compatible hydrogenated amorphous silicon waveguides," Optics Letters **36**, 552–554 (2011).

[29] C. Grillet, L. Carletti, C. Monat, P. Grosse, B. Ben Bakir, S. Menezo, J. M. Fedeli, and D. J. Moss, "Amorphous silicon nanowires combining high nonlinearity, FOM and optical stability," Opt. Express **20**, 22609–22615 (2012).

[30] J. Matres, G. C. Ballesteros, P. Gautier, J. M. Fédéli, J. Martí, and C. J. Oton, "High nonlinear figure-of-merit amorphous silicon waveguides," Opt. Express **21**, 3932–3940 (2013).

[31] K.-Y. Wang and A. C. Foster, "Ultralow power continuous-wave frequency conversion in hydrogenated amorphous silicon waveguides," Optics Letters **37**, 1331–1333 (2012).

[32] Q. Lin, O. J. Painter, and G. P. Agrawal, "Nonlinear optical phenomena in silicon waveguides: modeling and applications," Opt. Express **15**, 16604–16644 (2007).

[33] M. Nakazawa, T. Yamamoto, and K. R. Tamura, "1.28 Tbit/s-70 km OTDM transmission using third- and fourth-order simultaneous dispersion compensation with a phase modulator," Electronics Letters **36**, 2027–2029 (2000).

[34] T. D. Vo, H. Hu, M. Galili, E. Palushani, J. Xu, L. K. Oxenløwe, S. J. Madden, D. Y. Choi, D. A. P. Bulla, M. D. Pelusi, J. Schröder, B. Luther-Davies, and B. J. Eggleton, "Photonic chip based transmitter optimization and receiver demultiplexing of a 1.28 Tbit/s OTDM signal," Opt. Express **18**, 17252–17261 (2010).

[35] M. D. Pelusi, V. G. Ta'eed, M. R. E. Lamont, S. Madden, D. Y. Choi, B. Luther-Davies, and B. J. Eggleton, "Ultra-high nonlinear As2S3 planar waveguide for 160-Gb/s optical time-division demultiplexing by four-wave mixing," Photonics Technology Letters, IEEE **19**, 1496–1498 (2007).

[36] H. Ji, M. Pu, H. Hu, M. Galili, L. K. Oxenløwe, K. Yvind, J. r. M. Hvam, and P. Jeppesen, "Optical Waveform Sampling and Error-Free Demultiplexing of 1.28 Tb/s Serial Data in a Nanoengineered Silicon Waveguide," IEEE Journal of Lightwave Technology **29**, 426–431 (2011).

[37] F. Li, M. Pelusi, D. X. Xu, A. Densmore, R. Ma, S. Janz, and D. J. Moss, "Error-

free all-optical demultiplexing at 160Gb/s via FWM in a silicon nanowire," Opt. Express **18**, 3905–3910 (2010).

[38] E. Tangdiongga, Y. Liu, H. de Waardt, G. D. Khoe, A. M. J. Koonen, H. J. S. Dorren, X. Shu, and I. Bennion, "All-optical demultiplexing of 640 to 40 Gbits/s using filtered chirp of a semiconductor optical amplifier," Optics Letters **32**, 835–837 (2007).

[39] B. Corcoran, M. D. Pelusi, C. Monat, J. Li, L. O'Faolain, T. F. Krauss, and B. J. Eggleton, "Ultracompact 160 Gbaud all-optical demultiplexing exploiting slow light in an engineered silicon photonic crystal waveguide," Optics Letters **36**, 1728–1730 (2011).

[40] A. Martinez, J. Blasco, P. Sanchis, J. V. Galan, J. Garcia-Ruperez, E. Jordana, P. Gautier, Y. Lebour, S. Hernandez, R. Spano, R. Guider, N. Daldosso, B. Garrido, J. M. Fedeli, L. Pavesi, and J. Marti, "Ultrafast all-optical switching in a silicon-nanocrystal-based silicon slot waveguide at telecom wavelengths," Nano Letters **10**, 1506–1511 (2010).

[41] K. Nozaki, T. Tanabe, A. Shinya, S. Matsuo, T. Sato, H. Taniyama, and M. Notomi, "Sub-femtojoule all-optical switching using a photonic-crystal nanocavity," Nat Photon **4**, 477–483 (2010).

[42] C. Koos, P. Vorreau, T. Vallaitis, P. Dumon, W. Bogaerts, R. Baets, B. Esembeson, I. Biaggio, T. Michinobu, F. Diederich, W. Freude, and J. Leuthold,

"All-optical high-speed signal processing with silicon-organic hybrid slot waveguides," Nat Photon **3**, 216–219 (2009).

[43] K. G. Petrillo and M. A. Foster, "Scalable ultrahigh-speed optical transmultiplexer using a time lens," Optics Express **19**, 14051–14059 (2011).

[44] H. C. Hansen Mulvad, E. Palushani, H. Hu, H. Ji, M. Lillieholm, M. Galili, A. T. Clausen, M. Pu, K. Yvind, J. r. M. Hvam, P. Jeppesen, and L. K. Oxenløwe, "Ultra-high-speed optical serial-to-parallel data conversion by time-domain optical Fourier transformation in a silicon nanowire," Opt. Express **19**, B825–B835 (2011).

[45] E. Palushani, H. C. H. Mulvad, M. Galili, H. Hao, L. K. Oxenlowe, A. T. Clausen, and P. Jeppesen, "OTDM-to-WDM conversion based on time-to-frequency mapping by time-domain optical fourier transformation," Selected Topics in Quantum Electronics, IEEE Journal of **18**, 681–688 (2012).

[46] E. Ciaramella, "Wavelength Conversion and All-Optical Regeneration: Achievements and Open Issues," Lightwave Technology, Journal of **30**, 572–582 (2012).

[47] S. Radic, C. J. McKinstrie, R. M. Jopson, J. C. Centanni, and A. R. Chraplyvy, "All-optical regeneration in one- and two-pump parametric amplifiers using highly nonlinear optical fiber," Photonics Technology Letters, IEEE **15**, 957–959 (2003).

[48] H. Simos, A. Bogris, and D. Syvridis, "Investigation of a 2R all-optical regenerator based on four-wave mixing in a semiconductor optical amplifier," Lightwave Technology, Journal of **22**, 595–604 (2004).

[49] E. Ciaramella, F. Curti, and S. Trillo, "All-optical signal reshaping by means of four-wave mixing in optical fibers," Photonics Technology Letters, IEEE **13**, 142–144 (2001).

[50] P. V. Mamyshev, "All-optical data regeneration based on self-phase modulation effect," in "Optical Communication, 1998. 24th European Conference on," , vol. 1 (1998), vol. 1, pp. 475–476 vol.1.

[51] M. Rochette, F. Libin, V. Ta'eed, D. J. Moss, and B. J. Eggleton, "2R optical regeneration: an all-optical solution for BER improvement," Selected Topics in Quantum Electronics, IEEE Journal of **12**, 736–744 (2006).

[52] M. Rochette, J. N. Kutz, J. L. Blows, D. Moss, J. T. Mok, and B. J. Eggleton, "Bit-error-ratio improvement with 2R optical regenerators," Photonics Technology Letters, IEEE **17**, 908–910 (2005).

[53] S. J. Madden, D. Y. Choi, D. A. Bulla, A. V. Rode, B. Luther-Davies, V. G. Ta'eed, M. D. Pelusi, and B. J. Eggleton, "Long, low loss etched As2S3 chalcogenide waveguides for all-optical signal regeneration," Opt. Express **15**, 14414–14421 (2007).

[54] R. Salem, M. A. Foster, A. C. Turner, D. F. Geraghty, M. Lipson, and A. L. Gaeta, "All-optical regeneration on a silicon chip," Opt. Express **15**, 7802–7809 (2007).

[55] L. Fu, M. Rochette, V. Ta'eed, D. Moss, and B. Eggleton, "Investigation of self-phase modulation based optical regeneration in single mode As2Se3 chalcogenide glass fiber," Opt. Express **13**, 7637–7644 (2005).

[56] H. G. Weber, R. Ludwig, S. Ferber, C. Schmidt-Langhorst, M. Kroh, V. Marembert, C. Boerner, and C. Schubert, "Ultrahigh-Speed OTDM-Transmission Technology," Lightwave Technology, Journal of **24**, 4616–4627 (2006).

[57] T. Richter, E. Palushani, C. Schmidt-Langhorst, R. Ludwig, L. Molle, M. Nolle, and C. Schubert, "Transmission of Single-Channel 16-QAM Data Signals at Terabaud Symbol Rates," IEEE Journal of Lightwave Technology **30**, 504–511 (2012).

[58] H. C. H. Mulvad, L. K. Oxenlwe, M. Galili, A. T. Clausen, L. Gruner-Nielsen, and P. Jeppesen, "1.28 TBIT/s single-polarisation serial OOK optical data generation and demultiplexing," Electronics Letters **45**, 280–281 (2009).

[59] H. C. H. Mulvad, M. Galili, L. K. Oxenlø we, H. Hu, A. T. Clausen, J. B. Jensen, C. Peucheret, and P. Jeppesen, "Demonstration of 5.1 Tbit/s data capacity on a single-wavelength channel," Optics Express **18**, 1438–1443 (2010).

[60] M. Nakazawa, T. Hirooka, P. Ruan, and P. Guan, "Ultrahigh-speed "orthogonal" TDM transmission with an optical Nyquist pulse train," Optics Express **20**, 1129–1140 (2012).

[61] HillerkussD, SchmogrowR, SchellingerT, JordanM, WinterM, HuberG, VallaitisT, BonkR, KleinowP, FreyF, RoegerM, KoenigS, LudwigA, MarculescuA, LiJ, HohM, DreschmannM, MeyerJ, S. Ben Ezra, NarkissN, NebendahlB, ParmigianiF, PetropoulosP, ResanB, OehlerA, WeingartenK, EllermeyerT, LutzJ, MoellerM, HuebnerM, BeckerJ, KoosC, FreudeW, LeutholdJ, and D. Hillerkuss et al, "26 Tbit s-1 line-rate super-channel transmission utilizing all-optical fast Fourier transform processing," Nat Photon **5**, 364–371 (2011).

[62] Y. Yang, M. Foster, J. B. Khurgin, and A. B. Cooper, "Heterodyne detection using spectral line pairing for spectral phase encoding optical code division multiple access and dynamic dispersion compensation," Opt. Express **20**, 17600–17609 (2012).

[63] B. P. Kuo, E. Myslivets, N. Alic, and S. Radic, "Wavelength Multicasting via Frequency Comb Generation in a Bandwidth-Enhanced Fiber Optical Parametric Mixer," Lightwave Technology, Journal of **29**, 3515–3522 (2011).

[64] C. Dorrer, "High-speed measurements for optical telecommunication systems," Selected Topics in Quantum Electronics, IEEE Journal of **12**, 843–858 (2006).

[65] M. Kahrs, "50 years of RF and microwave sampling," Microwave Theory and Techniques, IEEE Transactions on **51**, 1787–1805 (2003).

[66] M. A. Duguay and J. W. Hansen, "An ultrafast light gate," Applied Physics Letters **15**, 192–194 (1969).

[67] G. Vogel, A. Savage, and M. Duguay, "Picosecond optical sampling," Quantum Electronics, IEEE Journal of **10**, 642–646 (1974).

[68] R. Trebino, K. W. DeLong, D. N. Fittinghoff, J. N. Sweetser, M. A. Krumbugel, B. A. Richman, and D. J. Kane, "Measuring ultrashort laser pulses in the time-frequency domain using frequency-resolved optical gating," Review of Scientific Instruments **68**, 3277–3295 (1997).

[69] R. Trebino, *Frequency resolved optical gating: the measurement of ultrashort laser pulses* (Kluwer Academic Publishers, 2000).

[70] C.-S. Hsu, H.-C. Chiang, H.-P. Chuang, C.-B. Huang, and S.-D. Yang, "Forty-photon-per-pulse spectral phase retrieval by shaper-assisted modified interferometric field autocorrelation," Optics Letters **36**, 2611–2613 (2011).

[71] C. Iaconis and I. A. Walmsley, "Spectral phase interferometry for direct electric-field reconstruction of ultrashort optical pulses," Optics Letters **23**, 792–794 (1998).

[72] P. O'Shea, M. Kimmel, X. Gu, and R. Trebino, "Highly simplified device for ultrashort-pulse measurement," Optics Letters **26**, 932–934 (2001).

[73] T. Taira and K. Kikuchi, "Highly sensitive frequency-resolved optical gating in 1.55 μm region using organic nonlinear optical crystal for second-harmonic generation," Electronics Letters **36**, 1719–1720 (2000).

[74] J. Fatome, S. Pitois, and G. Millot, "Sensitivity of SHG-FROG for the characterization of ultrahigh-repetition-rate telecommunication laser sources," Optical Fiber Technology **10**, 73–78 (2004).

[75] I. Amat-Roldán, I. Cormack, P. Loza-Alvarez, E. Gualda, and D. Artigas, "Ultrashort pulse characterisation with SHG collinear-FROG," Optics Express **12**, 1169–1178 (2004).

[76] P.-A. Lacourt, J. M. Dudley, J.-M. Merolla, H. Porte, J.-P. Goedgebuer, and W. T. Rhodes, "Milliwatt-peak-power pulse characterization at 1.55 m by wavelength-conversion frequency-resolved optical gating," Optics Letters **27**, 863–865 (2002).

[77] P. A. Lacourt, M. Hanna, and J. M. Dudley, "Broad-band and ultrasensitive pulse characterization using frequency-resolved optical gating via four-wave mixing in a semiconductor optical amplifier," Photonics Technology Letters, IEEE **17**, 157–159 (2005).

[78] S.-D. Yang, A. M. Weiner, K. R. Parameswaran, and M. M. Fejer, "Ultrasensitive second-harmonic generation frequency-resolved optical gating by aperiodically poled LiNbO3 waveguides at 1.5 m," Optics Letters **30**, 2164–2166 (2005).

[79] J. Prawiharjo, F. Parmigiani, K. Gallo, P. Petropoulos, N. G. Broderick, and D. J. Richardson, "Cascaded-chi(2)-interaction-based frequency-resolved optical gating in a periodically poled LiNbO3 waveguide," Optics Letters **31**, 244–246 (2006).

[80] M. A. Foster, R. Salem, D. F. Geraghty, A. C. Turner, M. Lipson, and A. L. Gaeta, "Frequency-Resolved Optical Gating on a Silicon Photonic Chip," (Optical Society of America, 2008), p. CMC4.

[81] K.-Y. Wang, K. G. Petrillo, M. A. Foster, A. C. Foster, P. K. G., F. M. A., F. A. C., K. G. Petrillo, M. A. Foster, and A. C. Foster, "Highly-Sensitive Ultrafast Pulse Characterization Utilizing Four-wave Mixing in an Amorphous Silicon Nanowaveguide," in "Conference on Lasers and Electro-Optics (CLEO)," (Optical Society of America, San Jose, California, 2013), p. CW1H.6.

[82] D. Meshulach, Y. Barad, and Y. Silberberg, "Measurement of ultrashort optical pulses by third-harmonic generation," Journal of the Optical Society of America B **14**, 2122–2125 (1997).

[83] G. Ramos-Ortiz, M. Cha, S. Thayumanavan, J. Mendez, S. R. Marder, and

B. Kippelen, "Ultrafast-pulse diagnostic using third-order frequency-resolved optical gating in organic films," Applied Physics Letters **85**, 3348–3350 (2004).

[84] S. K. Das, C. Schwanke, A. Pfuch, W. Seeber, M. Bock, G. Steinmeyer, T. Elsaesser, and R. Grunwald, "Highly efficient THG in TiO2 nanolayers for third-order pulse characterization," Optics Express **19**, 16985–16995 (2011).

[85] P. Devgan, T. Renyong, V. S. Grigoryan, and P. Kumar, "Highly efficient multichannel wavelength conversion of DPSK signals," Lightwave Technology, Journal of **24**, 3677–3682 (2006).

[86] L. Xu, N. Ophir, M. Menard, R. K. W. Lau, A. C. Turner-Foster, M. A. Foster, M. Lipson, A. L. Gaeta, and K. Bergman, "Simultaneous wavelength conversion of ASK and DPSK signals based on four-wave-mixing in dispersion engineered silicon waveguides," Opt. Express **19**, 12172–12179 (2011).

[87] Y. Wei, S. Howard, A. Straub, Z. Wang, J. Cheng, S. Gao, and C. Xu, "High sensitivity third-order autocorrelation measurement by intensity modulation and third harmonic detection," Optics Letters **36**, 2372–2374 (2011).

[88] M. A. Foster, A. C. Turner, J. E. Sharping, B. S. Schmidt, M. Lipson, and A. L. Gaeta, "Broad-band optical parametric gain on a silicon photonic chip," Nature **441**, 960 (2006).

[89] B. Jalali, V. Raghunathan, D. Dimitropoulos, and O. Boyraz, "Raman-based

silicon photonics," Selected Topics in Quantum Electronics, IEEE Journal of **12**, 412–421 (2006).

[90] B. Kuyken, X. Liu, G. Roelkens, R. Baets, J. R. M. Osgood, and W. M. J. Green, "50 dB parametric on-chip gain in silicon photonic wires," Optics Letters **36**, 4401–4403 (2011).

[91] H. Rong, S. Xu, Y.-H. Kuo, V. Sih, O. Cohen, O. Raday, and M. Paniccia, "Low-threshold continuous-wave Raman silicon laser," Nature Photon. **1**, 232 (2007).

[92] A. Gajda, L. Zimmermann, M. Jazayerifar, G. Winzer, H. Tian, R. Elschner, T. Richter, C. Schubert, B. Tillack, and K. Petermann, "Highly efficient cw parametric conversion at 1550 nm in soi waveguides by reverse biased p-i-n junction," Optics Express **20**, 13100–13107 (2012).

[93] X. P. Liu, R. M. Osgood, Y. A. Vlasov, and W. M. J. Green, "Mid-infrared optical parametric amplifier using silicon nanophotonic waveguides," Nature Photonics **4**, 557–560 (2010).

[94] K.-Y. Wang and A. C. Foster, "Broad-bandwidth Near-IR Parametric Amplification in Amorphous Silicon Waveguides," in "Conference on Lasers and Electro-Optics (CLEO)," (Optical Society of America, San Jose, California, 2013), p. QTh4E.4.

[95] H. Rong, S. Xu, O. Cohen, O. Raday, M. Lee, V. Sih, and M. Paniccia, "A cascaded silicon Raman laser," Nat Photon **2**, 170–174 (2008).

[96] Y. Zhou, K. Cheung, S. Yang, P. Chui, and K.-Y. Wong, "A time-dispersion-tuned picosecond fiber-optical parametric oscillator," Photonics Technology Letters, IEEE **21**, 1223–1225 (2009).

[97] L. Zhang, S. Yang, P. Li, X. Wang, D. Gou, W. Chen, W. Luo, H. Chen, M. Chen, and S. Xie, "An all-fiber continuously time-dispersion-tuned picosecond optical parametric oscillator at 1 μm region," Opt. Express **21**, 25167–25173 (2013).

[98] R. Ahmad and M. Rochette, "Chalcogenide optical parametric oscillator," Opt. Express **20**, 10095–10099 (2012).

[99] J. E. Sharping, M. A. Foster, A. L. Gaeta, J. Lasri, O. Lyngnes, and K. Vogel, "Octave-spanning, high-power microstructure-fiber-based optical parametric oscillators," Opt. Express **15**, 1474–1479 (2007).

[100] J. F. Bauters, M. L. Davenport, M. J. R. Heck, J. K. Doylend, A. Chen, A. W. Fang, and J. E. Bowers, "Silicon on ultra-low-loss waveguide photonic integration platform," Opt. Express **21**, 544–555 (2013).

[101] J. E. Sharping, K. F. Lee, M. A. Foster, A. C. Turner, B. S. Schmidt, M. Lipson,

A. L. Gaeta, and P. Kumar, "Generation of correlated photons in nanoscale silicon waveguides," Opt. Express **14**, 12388–12393 (2006).

[102] K.-i. Harada, H. Takesue, H. Fukuda, T. Tsuchizawa, T. Watanabe, K. Yamada, Y. Tokura, and S.-i. Itabashi, "Generation of high-purity entangled photon pairs using silicon wirewaveguide," Opt. Express **16**, 20368–20373 (2008).

[103] K. Harada, H. Takesue, H. Fukuda, T. Tsuchizawa, T. Watanabe, K. Yamada, Y. Tokura, and S. Itabashi, "Frequency and Polarization Characteristics of Correlated Photon-Pair Generation Using a Silicon Wire Waveguide," Selected Topics in Quantum Electronics, IEEE Journal of **16**, 325–331 (2010).

[104] S. Clemmen, A. Perret, S. K. Selvaraja, W. Bogaerts, D. van Thourhout, R. Baets, P. Emplit, and S. Massar, "Generation of correlated photons in hydrogenated amorphous-silicon waveguides," Optics Letters **35**, 3483–3485 (2010).

[105] H. Takesue and K. Inoue, "1.5-μm band quantum-correlated photon pair generation in dispersion-shifted fiber: suppression of noise photons by cooling fiber," Opt. Express **13**, 7832–7839 (2005).

[106] Q. Lin, F. Yaman, and G. P. Agrawal, "Photon-pair generation in optical fibers through four-wave mixing: Role of Raman scattering and pump polarization," Physical Review A **75**, 23803 (2007).

[107] S. Wang and G. Kanter, "Robust multiwavelength all-fiber source of

polarization-entangled photons with built-in analyzer alignment signal," Selected Topics in Quantum Electronics, IEEE Journal of **15**, 1733–1740 (2009).

Vita

Ke-Yao Wang graduated from National Taiwan University with a B.S. (2005) and M.S. (2007) in physics and electronics engineering, respectively. Then he enrolled in Department of Electrical and Computer Engineering at Johns Hopkins University in 2009. His research focuses on Si Photonics, nonlinear optics, and integrated optics. During his PhD study, he has won first, second and third price in student poster competition in optics and photonics held in University in Maryland in 2013, 2014 and 2012, respectively. His work appears in Optics Letters and Optics Express. He has given more than 10 conference talks and seminars during his PhD study.